

This is a peer reviewed preprint. It has been submitted to Minerals Engineering and accepted.

Anna Vanderbruggen^{1,3}, Eligiusz Gugala², Rosie Blannin¹, Kai Bachmann¹, Rodrigo Serna-Guerrero³, Martin Rudolph¹*

¹ Helmholtz Zentrum Dresden Rossendorf (HZDR), Helmholtz Institute Freiberg for Resource Technology (HIF), Chemnitz Straße 40, 09599 Freiberg, Germany

² TESCAN ORSAY HOLDING, a.s., Libušina třída 21, 623 00 Brno, Czech Republic

³ Department of Chemical and Metallurgical Engineering, School of Chemical Engineering, Aalto University, P.O. Box 16200, 00076 Aalto, Finland

** Corresponding author. Email address: a.vanderbruggen@hzdr.de*

Automated mineralogy as a novel approach for the compositional and textural characterization of spent lithium-ion batteries

Anna Vanderbruggen^{1,3*}, Eligiusz Gugala², Rosie Blannin¹, Kai Bachmann¹, , Rodrigo Serna-Guerrero³, Martin Rudolph¹

¹ Helmholtz Zentrum Dresden Rossendorf (HZDR), Helmholtz Institute Freiberg for Resource Technology (HIF), Chemnitz Straße 40, 09599 Freiberg, Germany

² TESCAN ORSAY HOLDING, a.s., Libušina třída 21, 623 00 Brno, Czech Republic

³ Department of Chemical and Metallurgical Engineering, School of Chemical Engineering, Aalto University, P.O. Box 16200, 00076 Aalto, Finland

* Corresponding author. Email address: a.vanderbruggen@hzdr.de

Keywords: Automated mineralogy, black mass, characterization, liberation, lithium-ion batteries, recycling, mineral processing

Abstract

Mechanical recycling processes aim to separate particles based on their physical properties, such as size, shape and density, and physico-chemical surface properties, such as wettability. Secondary materials, including electronic waste, are highly complex and heterogeneous, which complicates recycling processes. In order to improve recycling efficiency, characterization of both recycling process feed materials and intermediate products is crucial. Textural characteristics of particles in waste mixtures cannot be determined by conventional characterization techniques, such as X-ray fluorescence and X-ray diffraction spectroscopy. This paper presents the application of automated mineralogy as an analytical tool, capable of describing discrete particle characteristics for monitoring and diagnosis of lithium ion battery (LIB) recycling approaches. Automated mineralogy, which is well established for the analysis of primary raw materials but has not yet been tested on battery waste, enables the acquisition of textural and chemical information, such as elemental and phase composition, morphology, association and degree of liberation. For this study, a thermo-mechanically processed black mass (< 1 mm fraction) from spent LIBs was characterized with automated mineralogy. Each particle was categorized based on which LIB component it comprised: Al foil, Cu foil, graphite, lithium metal oxides and alloys from casing. A more selective liberation of the anode components was achieved by thermo-mechanical treatment, in comparison to the cathode components. Therefore, automated mineralogy can provide vital information for understanding the properties of black mass particles, which determine the success of mechanical recycling processes. The introduced methodology is not limited to the presented case study and is applicable for the optimization of different separation unit operations in recycling of waste electronics and batteries.

1. Introduction

Lithium-ion batteries (LIBs) rapidly became the dominant electrochemical power source for portable electronics since their commercialization in the 1990's, due to their high energy density (Blomgren, 2017; Evertz et al., 2015; Yoshio and Noguchi, 2009). Many devices use these batteries, including consumer electronics, such as mobile phones and laptops, hybrid and electric vehicles, and stationary storage applications (Manthiram, 2017). The average life-span of a consumer electronic LIB is approximately 2 years (Gu et al., 2017; W. Zhang et al., 2018), while electric vehicle batteries have an estimated life-span of around 10 years (Chen et al., 2019; Or et al., 2020). Considering that LIBs have been in use for 30 years, and their production volume continues to increase, it is reasonable to forecast a considerable growth of end-of-life LIB streams in the foreseeable future.

Recycling processes aim to separate and recover components with high economic value. To recognize the challenges faced in the separation of LIB components, it is essential to understand their design and internal structure (Figure 1). Typically, LIBs comprise cells, which include a cathode and anode, separated by a polymer separator. Both electrodes consist of a conductive foil, coated by active particles. Most commonly, the anode comprises Cu foils and spheroidized natural graphite or synthetic graphite

particles (Writer, 2019). The cathode is usually made of lithium metal oxides particles on Al foil. However, unlike the anode materials, there is a wide diversity of cathode chemistries used in commercial LIBs, such as LiCoO_2 (LCO), LiMn_2O_4 (LMO), LiNiCoAlO_2 (NCA), LiFePO_4 (LFP), LiTiO_2 (LTO) and variable stoichiometry of LiNiMnCoO_2 (NMC) (Manthiram, 2020; Warner, 2015). The cell components (foils, graphite particles/lithium metal oxides) are tightly packed and adhered together by an organic binder, such as polyvinylidene fluoride (PVDF) for the cathode (Mekonnen et al., 2016) and Styrene Butadiene Rubber/Sodium Carboxymethyl Cellulose (SBR/Na-CMC) for the anode (Bresser et al., 2018; Wang et al., 2012).

As Figure 1 shows, the complex structure of LIBs renders the separation of the different components highly challenging. For instance, the presence of binder complicates the liberation of active particles from the foils, reducing the liberation efficiency during the recycling process (Widijatmoko et al., 2020; Zhang et al., 2019a). Extended mechanical processes required to liberate more active particles and counter the effects of the binder may result in undesired foil particles in the fine fraction, which can be problematic in subsequent recycling steps (Diekmann et al., 2017; Werner et al., 2020). The efficiency of any hydrometallurgical process is affected by the chemical composition of the feed. For example, Cu traces present during Ni precipitation are co-precipitated, effectively resulting in Ni losses and a reduction of purity (Velázquez-Martínez et al., 2019; Zou et al., 2013). The diversity of cathode chemistry poses yet another challenge for recycling processes since different battery chemistries may require specific conditions for an efficient recycling process (Velázquez-Martínez et al., 2019). Therefore, knowing the chemical composition and the ratio of cathode chemistry used as an input in hydrometallurgical processes would greatly help when determining optimum process conditions (Or et al., 2020).

For the reasons mentioned above, accurate characterization of spent LIBs is crucial for monitoring and improving the efficiency of recycling processes. However, the analyses required to accurately characterize these materials are complex as each recycling feed and recycling product is unique. Moreover, there is a huge diversity of materials in a LIB, including metals, oxides, inorganic or organic components. The literature offers examples of spent LIB characterization using X-Ray Fluorescence (XRF), Inductively Coupled Plasma Mass Spectrometry (ICP-MS), Energy Dispersive X-ray Spectroscopy (EDX) coupled with electron microscopy, thermal gravimetric analysis (TGA) and X-ray Powder Diffraction (XRD) (Lu et al., 2017; Shi et al., 2018; Wang et al., 2012; Widijatmoko et al., 2020). However, these techniques do not discriminate between the individual particle properties within the sample mixture. Recently, Zielinski *et al.* (2020) developed a multi-analytical methodology for industrial samples of spent Ni-MH battery powders. They succeeded in identifying and quantifying three type of particles in the size fraction below 100 μm , by using statistical analysis based on clustering algorithms of an electron probe micro-analysis (EPMA) compositional map of the following elements Ni, Ce, Co, Fe, La, Mn, Nd, and O.

In contrast Scanning Electron Microscopy (SEM)-based automated mineralogy is a particle-based analysis that is widely used for primary resources and has been regularly demonstrated to be beneficial for process improvements (Buchmann et al., 2018; Gottlieb, 2008; Kupka et al., 2020; Pereira et al., 2019). However, to the best of the authors' knowledge, this valuable technique has not yet been applied to spent LIB materials. Automated mineralogy techniques involve high-resolution backscattered electron imaging, combined with EDX spectroscopy, to identify and segment particles and determine their chemical composition based on their characteristic X-ray spectra. Quantitative information on a wide range of properties can be obtained with this technique, such as modal phase content, bulk chemistry, size and phase associations of the analyzed sample as a function of the density, chemistry and surface area (Gu, 2003).

Automated mineralogy has the benefits of being a non-destructive method which is capable of analyzing a broad range of particle sizes, from a few microns up to a few centimeters. Additionally, different forms of sample materials can be analyzed, from particulate materials suspended in epoxy resin, often termed "grain mounts", to polished blocks and thin sections. In this study, iodized epoxy resin was used for the preparation of grain mounts of the studied material, in order to allow the analysis of carbon phases, which are typically not quantified in black mass characterization, according to Zielinski *et al.* (2020).

However, the application of automated mineralogy to secondary materials, which could also be termed "Automated Materials Characterization" (Schulz et al., 2020) since secondary materials are not typically

comprised of minerals, encounters significant challenges. The characterization of primary resources is enabled by the existing knowledge of mineral phases. Mineral reference lists, including X-ray spectra, composition, and densities of mineral phases, are required for the reliable identification of components under study by automated mineralogy systems (Hrstka et al., 2018). This knowledge is largely missing for secondary materials, such as LIBs. The compilation of the required reference data is not straightforward for these highly heterogeneous and complex materials, would be costly and time-consuming, and requires a deep understanding of the secondary materials in question, in addition to an understanding of automated mineralogy. Recently, Sandmann *et al.* (2019) reported the use of automated mineralogy to characterize crushed mobile phones. With the sample being made not of minerals, but secondary materials, they had to create a data base. This data base consisted of 130 compounds. The results showed that 10 of the compounds accounted for 60 to 70 wt.% of the total sample and the 120 remaining compounds represented 30 to 40 wt.%. More than 100 compounds occurred in amounts of less than 1 wt.% each, which clearly highlights the complex composition of such secondary materials.

Despite the many difficulties when applied to secondary materials, automated mineralogy can provide highly useful information. Therefore, it is worthwhile to continue developing the application of these methods, towards becoming a norm for analyzing such materials. The present study demonstrates the application of automated mineralogical analysis for the fine fraction (< 1 mm) of different spent LIBs, a mixed fraction typically referred to as the “black mass”. Components were defined at the level of functional form of the chemical compounds used in LIBs (Al foil, Cu foil, casing, lithium metal oxides and graphite) and each particle of the sample was categorized according to the LIB component(s) which it comprised. Information on the chemical composition, morphology and the degree of liberation of the LIB components was acquired, helping to understand how the particles behaved during the mechanical process and to determine the success of these processes. The introduced methodology is not limited to the presented case study and is applicable for the optimization of different separation unit operations.

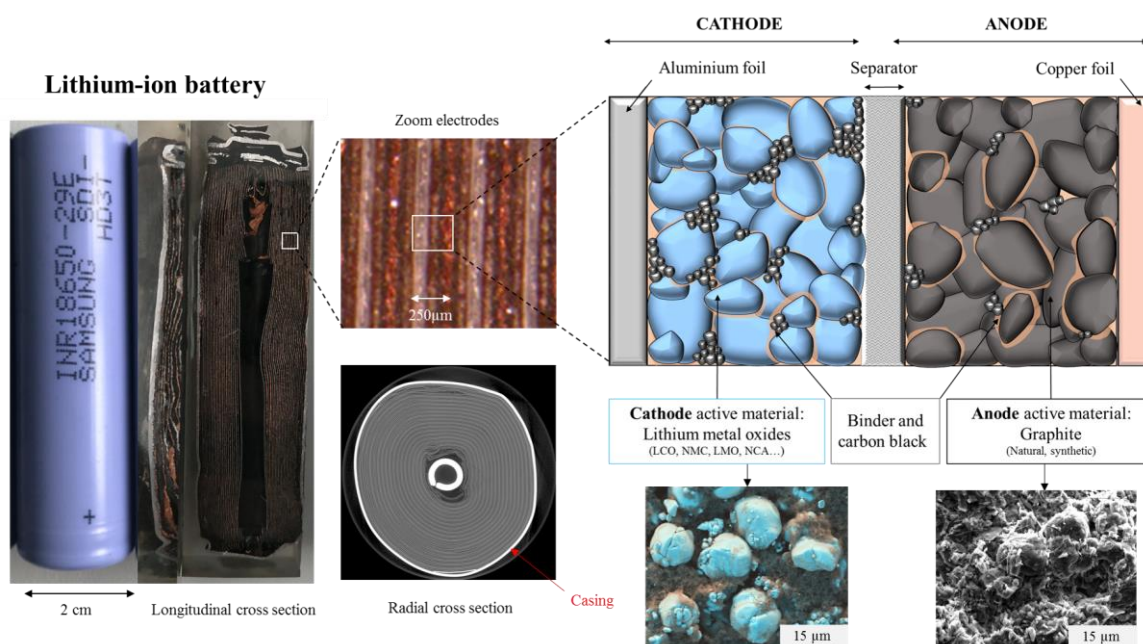


Figure 1 Details of a lithium-ion battery. Left: images of an 18650 type LIB. Top right: schema of a LIB cell design and composition. Bottom right: SEM image of LCO with binder and natural spheroidized graphite with binder.

2. Materials and Methods

2.1. Sample preparation

For this study, a black mass sample was provided by an industrial scale operator, Accurec Recycling GmbH. The spent LIBs were sorted by chemistry, and a mixture of NMC and LCO were used as a feed for this recycling process. The studied black mass was produced by pyrolysis, dry crushing and sieving of spent LIBs as illustrated in Figure 2 A. The vacuum pyrolysis stage was conducted at 500-600 °C. The thermal product was crushed and subsequently sieved through 1 mm openings.

The reliability of characterization results is highly dependent on the representativity of the samples (Gy, 1994). The sampling of black mass is challenging due to the heterogeneity of the particles in terms of both shape and density. For instance, graphite has a density of 2.2 g/cm^3 , while LiCoO_2 has a density of 5.05 g/cm^3 and Cu an even higher density of 8.9 g/cm^3 (Akimoto et al., 1998; Chehreh Chelgani et al., 2016; Cheng et al., 2017). Consequently, the sampling procedure was carefully designed to obtain the most homogenous sample for this characterization study (Figure 2 B). The 9.6 kg of black mass was manually homogenized and split into two sub-samples with the coning and quartering method, at the Helmholtz Institute Freiberg (HIF). A 4.8 kg sub-sample (A) was further split with a riffle splitter (Retsch PT100, Germany) to obtain samples of 200 g. One sub-sample of 200 g (B) was sieved with a vibratory column sieve (Fritsch Analysette 3, Idar-Oberstein, Germany) into four size fractions for further investigation: 500-1000 μm , 125-500 μm , 63-125 μm and < 63 μm .

For each of the 4 samples, a representative sub-sample was obtained with a rotary sample splitter (Retsch PT100, Retsch GmbH, Haan, Germany) for subsequent analytical investigations. The conducted analytical program comprises automated mineralogy (1.5 g), XRF (10 g) and elemental assay for C (1 g).

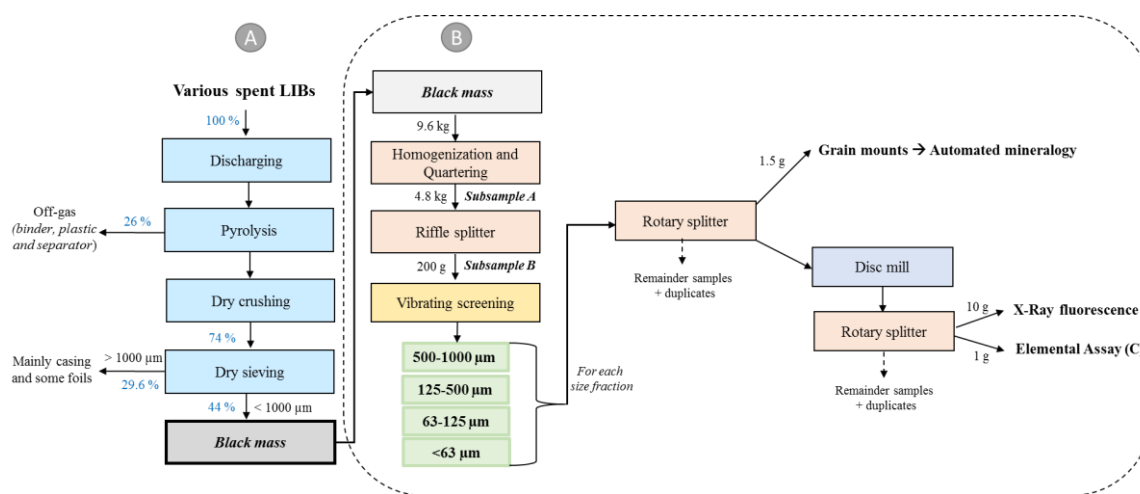


Figure 2 Simplified flowsheet of black mass production (A) and sample preparation for conducted analysis (B), in green are the 4 characterized samples.

For this study, carbon analysis is crucial due to the presence of graphite particles. However, as reported in several studies, automated mineralogy cannot distinguish graphite from epoxy resin (Sandmann and Gutzmer 2013; Sandmann et al., 2014; Rahfeld and Gutzmer 2017), which is typically used for grain mount sample preparation and has a very similar average atomic number to graphite. Therefore, the 4 grain mounts were prepared at HIF by using a method modified to suit the specific material studied, after Rahfeld and Gutzmer (2017). The particles were embedded in an iodized epoxy resin, which is a mixture of epoxy resin (301/1LB/A and 301/1LB/B from EPO-TEK, USA) and iodoform (CHI_3) with 99 wt.% purity (Alfa Aesar GmbH & Co KG, Karlsruhe, Germany), with a ratio of 10:1. With this iodized epoxy resin, a sufficient BSE contrast was obtained between all the particles (over 11.3%), including graphite (9.1 – 9.6%) and the surrounding medium (11.1 – 11.3%).

2.2. Automated mineralogy

Automated mineralogy combines high-resolution BSE images obtained by SEM with EDX measurements to determine the phase composition (volume or mass fraction) and geometrical parameters (e.g. size, shape, association) of particles on a polished surface. The first step was to acquire the BSE and X-ray analysis, and then to recognize and segment individual particles. The second step was the creation of a reference list, also called the “classification scheme”. The mineralogical phases of each particle were identified by matching the measured spectra to those in the reference list, which was previously created. The last step was the data processing, where the software calculates information such as modal phase content and phase associations of the analyzed sample as a function of density and

chemical composition (Bachmann et al., 2017; Fandrich et al., 2007; Kern et al., 2018). All these parameters can be further utilized for particle tracking techniques (Kupka et al., 2020).

2.2.1. Grain mount analysis

The analyses were carried out on a TIMA-X system at TESCAN in Brno, Czech Republic. The scanning electron microscope TIMA3 GMU is equipped with a field emission source (FEG) and SDD-EDS X-ray spectrometer (EDAX Element 30, with a calibration set point of 370 kcps) combined with Tescan Integrated Mineral Analyser (TIMA) software. The BSE signals were collected and used to determine the grain boundaries based on brightness contrasts. The analyzed surface was divided into a square grid, the X-ray acquisition was conducted at the analytical points imposed by the scanning modes. The 125 – 500 μm grain mount was analyzed with a high-resolution mapping acquisition mode to build the reference list. For the other grain mount, 500 – 1000 μm , 63 – 125 μm and < 63 μm , the dot mapping mode was used for acquisition time optimization. The operating conditions are listed in Table 1. Detailed information on the measurement modes is provided by Hrstka (2018) and Schulz *et al.* (2020).

Table 1 Parameters used during measurements

Parameters		
Acquisition mode	Dot mapping	High resolution mapping
Measurement type	Liberation analysis	Liberation analysis
Beam energy	15 kV	15 kV
Working distance	15.0 mm	15.0 mm
Pixel spacing	2 μm	4 μm
Dot spacing	6 μm	N/A

The identification of the chemical composition of particles detected during the data acquisition requires a reference list. However, no list was available for such secondary material and it was therefore the first focus of this study to develop a new reference list for this black mass, which could also be applied to other black mass from spent LIBs in order to identify the main LIB components. To that aim, a total of 55 spectra were collected in an iterative process. The first spectra collected and added to the reference list were from components which were easily distinguishable based on their macroscopic properties, e.g. backscatter electrons (BSE) level or morphologies, as given in Supplementary Data S1. The classification script, which matches the spectra from the reference list to the measured spectra, was run with the already collected spectra in order to locate the unclassified compounds (i.e. which do not match any spectra from the reference list) and allow the collection of more spectra to decrease the number of unknowns. This iterative approach was repeated until all of the main components were identified.

The following information was compiled for each item from the data base: 1) Name (usually based on the main elements by decreasing content, since they are chemical compounds or alloys rather than mineral phases), 2) Spectrum, 3) Density, and 4) Elemental composition. The density and elemental composition were calculated from the EDX spectrum. For the few remaining unknown spectra detected from a point or a segment, the auto-ID function was used to find the closest match of the unknown spectra to the one from the data base providing a phase identification. More information about this process is provided by Hrstka (2018).

2.2.2. Processing of automated mineralogy data

Data processing was performed using the TESCAN TIMA 1.6.73 software. Prior to the data processing, the mass percentage of the size fraction corresponding to each analyzed sample was introduced into the software. This was necessary because the samples were analyzed by size fractions (Figure 2) and required back calculations based on the mass balance in order to calculate bulk characteristics of the original black mass sample. For the black mass characterization, the mass balance was as follows: 9.1 wt.% for 500 – 1000 μm , 36.6 wt.% for 125 – 500 μm , 11.7 wt.% for 63 – 125 μm and 42.7 wt.% for the fraction below 63 μm .

The LIB components were defined at the level of functional form of the chemical compounds: Al foil, Cu foil, casing, lithium metal oxides and graphite. In order to simplify the data processing and reporting of results, the 55 collected spectra were grouped into 10 families based on the main element: Cu-bearing, Al-bearing, Co-bearing, Ni-bearing, Mn-bearing, MnNiCo-bearing, Si-bearing, C, Alloys (Fe/Si/Mn/Al/Cu) and Others. This grouping is illustrated in Figure 3 and was based on the knowledge of the chemical composition of LIB components, combined with a visual assessment of the spectra in different particles. Moreover, to simplify the data processing, the groups Co-bearing, Ni-bearing, Mn-bearing, MnNiCo-bearing were grouped as lithium metal oxides. The compositional thresholds can be found in Supplementary material S2.

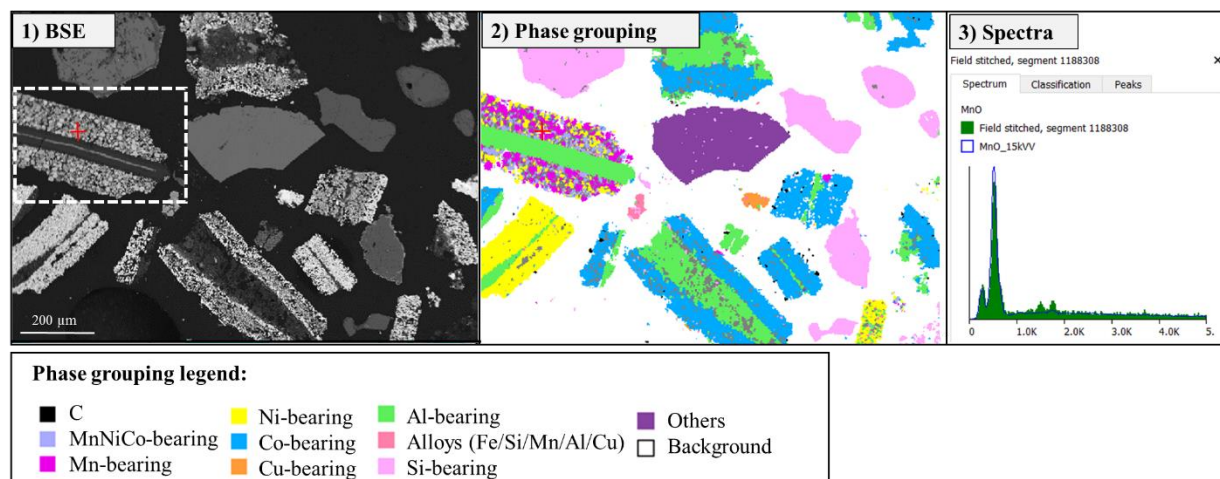


Figure 3 Automated mineralogy example showing the BSE image (1) and processed image (2) with grouping. The processed particle shown in (3) is the particle highlighted in (1), with the red cross marking point where the spectra was collected. This spectra (in green) clearly matches the MnO spectra from the reference list (blue line).

One particular challenge with secondary materials is that some phases can belong to more than one component. For instance, MnO can be identified in particles comprising lithium metal oxides (e.g. Figure 3), or in alloy particles from the casing. Hence, the grouping, which is only based on phases, is not sufficient to categorize the LIB components. Therefore, various categorizers were created to properly identify the LIB components. With the TIMA software, a categorizer is employed to subdivide particles composed of more than one phase. For this subdivision, a set of rules is imposed based on defined properties of the data objects, for instance particle size, liberation, phase contents, elemental content, etc. (Hrstka et al., 2018). A categorizer was developed to quantify the type of lithium metal oxides, LCO and NMC. For instance, LCO should not contain Mn or Ni, so for a particle to be categorized as LCO, the content of Mn-bearing and NiMnCo-bearing must be below 1 wt.%. The rules are detailed in Table 2.

Table 2 Lithium metal oxides categorizer

Lithium metal oxide type	Rules for the chemistry	Rules for the particles type
LCO – LiCoO_2	Mass wt.% of Co-bearing ≥ 10	Mass wt.% of Al-bearing ≤ 95 Mass wt.% of Alloys ≤ 30
	Mass wt.% of Mn-bearing ≤ 1 Mass wt.% of NiMnCo-bearing ≤ 1	
NMC – LiNiCoMnO_2	Mass wt.% of NiMnCo-bearing ≥ 10	
	Mass wt.% of Mn-bearing ≥ 1	
	Mass wt.% of Ni-bearing ≥ 1 Mass wt.% of Co-bearing ≤ 80	

For recycling processes, information on liberation and association of LIB components, based on free surface area, is important to model the theoretical behavior of components in a physical separation process. In this study, the liberation was defined at the LIB component level. In other words, when a particle was constituted of only one LIB component type (Al foil, Cu foil, lithium metal oxides and graphite), it was defined as liberated. Based on this definition, an aggregate of active particles is also

considered as liberated because it is composed of one type of LIB component, e.g. lithium metal oxides. The liberation and the locking are explained in the example shown in Figure 4. The particles on the left-hand side of Figure 4 are defined as non-liberated as they are composed of more than one LIB component type, Al foil and lithium metal oxides in this case. Such non-liberated particles can be further described by using the locking tool report from TIMA. For the locking analysis, a LIB component type was considered (e.g. Al foil) and the program selected each grain containing this targeted component. The program then analyzed the perimeter of the targeted grain and computed the length of the grain border that is free (red line in Figure 4) and the length of the border which is in contact with any other LIB component. For instance, using Figure 4 as an example, when selecting the Al foil component for locking analysis, 80% of the Al foil component is locked with lithium metal oxides and 20% of the border is free surface.

Moreover, during the grain mounts preparation, a common practice is to mix ultra-pure graphite with sample material to avoid touching particles (Røisi and Aasly, 2018). However, due to the importance of graphite analysis for this study, this method was not applied. If two particles were touching due to sample preparation, the automated touching-particle function on TIMA was applied, this function detects touching particles and processes them as separate particles (Hrstka et al., 2018).

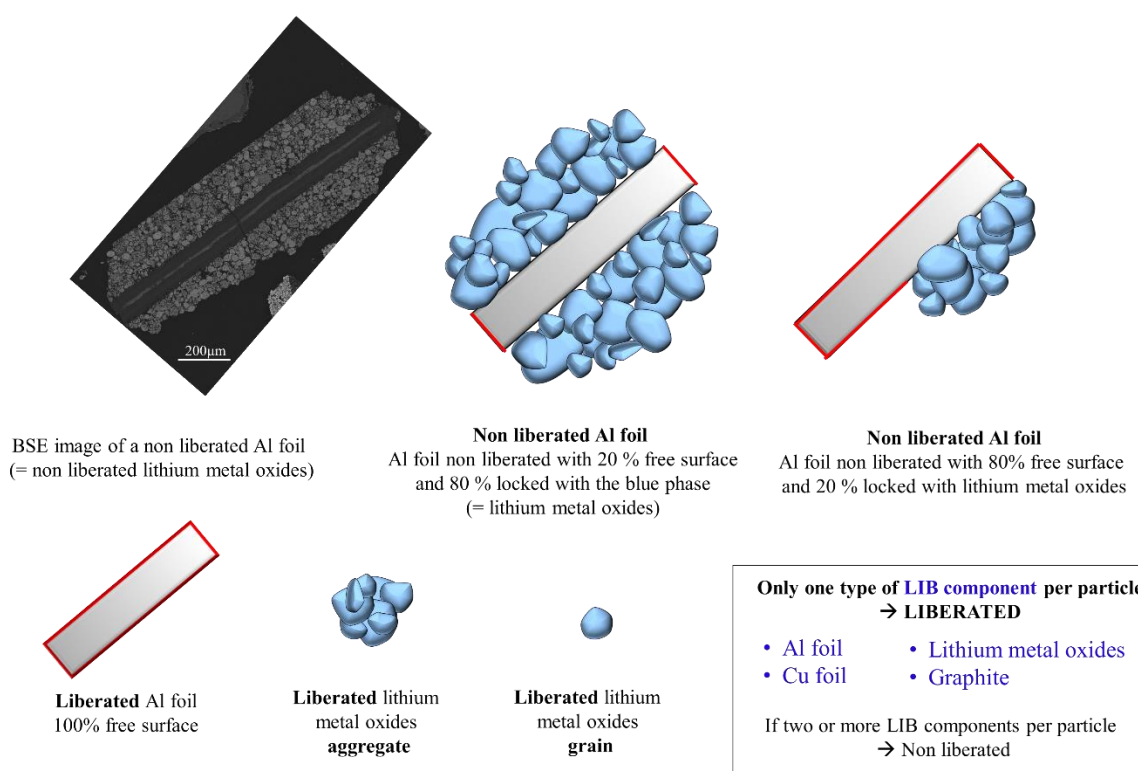


Figure 4 Example of liberation degree for an Al foil. The free surface is shown in the red line.

For calculating the liberation degree of LIB components, a categorizer was created in order to obtain data for Al foil, Cu foil, lithium metal oxides and graphite. With the liberation categorizer, each LIB component was divided into two categories: liberated and non-liberated. The liberation categorizer imposed rules on the free surface and chemistry of LIB components, detailed in Table 3. For a component to be considered as liberated, the free surface had to exceed 95%. This threshold value was chosen to provide some degree of flexibility for particles which, for example, were touching other particles and would therefore were incorrectly categorized. Based on the example of Figure 4, the particle is made of phases from the Al foil group and lithium metal oxides group and therefore this particle would be categorized as non-liberated Al foil.

Table 3 Liberation categorizer for LIB component

LIB component	Rules
Liberated Al foils	Mass wt.% of Al-bearing ≥ 95
	Mass wt.% of Lithium metal oxides ≥ 5
	Mass wt.% of Alloys ≤ 10
Liberated lithium metal oxides	Free surface wt.% Al-bearing ≥ 95
	Mass wt.% of Lithium metal oxides ≥ 80
	Mass wt.% of Al-bearing = 0
	Mass wt.% of Alloys ≤ 10
Liberated Cu foils	Free surface wt.% Lithium metal oxides ≥ 95
	Mass wt.% of Cu-bearing ≥ 95
	Mass wt.% of Alloys ≤ 10
Liberated graphite	Free surface wt.% Cu-bearing ≥ 95
	Mass wt.% of C ≥ 95
Non liberated Cu foils	Free surface wt.% of C ≥ 95
	Mass wt.% of Cu-bearing ≤ 10
Non liberated Al foils	Mass wt.% of Alloys ≤ 10
	Mass wt.% of Al-bearing ≥ 1
	Mass wt.% of Lithium metal oxides ≥ 1
	Mass wt.% of Alloys ≤ 10

In various articles on secondary material, the researchers calculated the degree of liberation of a component as a fraction of the number of liberated particles out of all the particles (Otsuki et al., 2020; Quan et al., 2012; Zhang and Forsberg, 1999; Zhu et al., 2011). This approach is not applicable for crushed lithium ion batteries in general, which contain too many fine particles. In particular, there are large amounts of fine and liberated Al foil particles, which do not contribute much to the overall content of Al foils, and therefore this method would result in an overestimation of the liberation degree. Hence, the liberation degree was based on the mass fraction of a component obtained by the liberation categorizer as displayed in Equation 2.

$$\text{Degree of Liberation} = \frac{\text{Mass \% of liberated component}}{\text{Total Mass\% of component}} \times 100 \quad (1)$$

2.3. Bulk chemical composition

The bulk chemical composition of all samples was measured to act as a quality control for the chemistry obtained by automated mineralogy. All samples were analyzed using XRF (Niton™ XL3t 980 from Thermo Scientific). An end-window X-ray tube with Gold-anode with a voltage of 8 kV to 50 kV. Light elements, with an atomic number below 11, cannot be accurately quantified by XRF. For these elements, it is difficult to ionize an atom with the photoelectric excitation and the produced signals are trapped within the sample itself (Kikongi *et al.*, 2017). The light elements, such as carbon, are of particular interest in this study and therefore it was necessary to quantify their composition with an alternative method. In order to complete the data validation, carbon analysis and fluorine were analyzed by the company ALS in Ireland. To determine the carbon content, the sample was leached with dilute hydrochloric acid to remove inorganic carbon. After filtering, washing, and drying, the remaining sample residue was roasted at 425 °C to remove organic carbon. The roasted residue was later analyzed for carbon in a high-temperature LECO furnace with infrared detection. In order to validate the assumptions made regarding the PVDF binder, the F content was measured using Na₂O₂ fusion, citric acid leach and ion selective electrode.

3. Results and discussion

3.1. Data validation

The black mass is complex in composition, consisting of a heterogeneous mix of elements, as displayed by the bulk chemistry presented in Figure 5. The fraction below 63 μm has a much higher carbon content than the other 3 fractions. The major elements (over 1 wt.%) detected are Al, C, Co, Cu, Fe, Mn, Al, Co, Ni, Si, with minor contents of other elements (over 0.1 wt.%), such as Ca, Cr, K, and Na. In addition, C was analyzed by the LECO method. The fraction “Others” in the Figure 5 comprises light elements which are not measurable with XRF, such as F, O and Li, as well as the element with contents less than 0.1 wt.%.

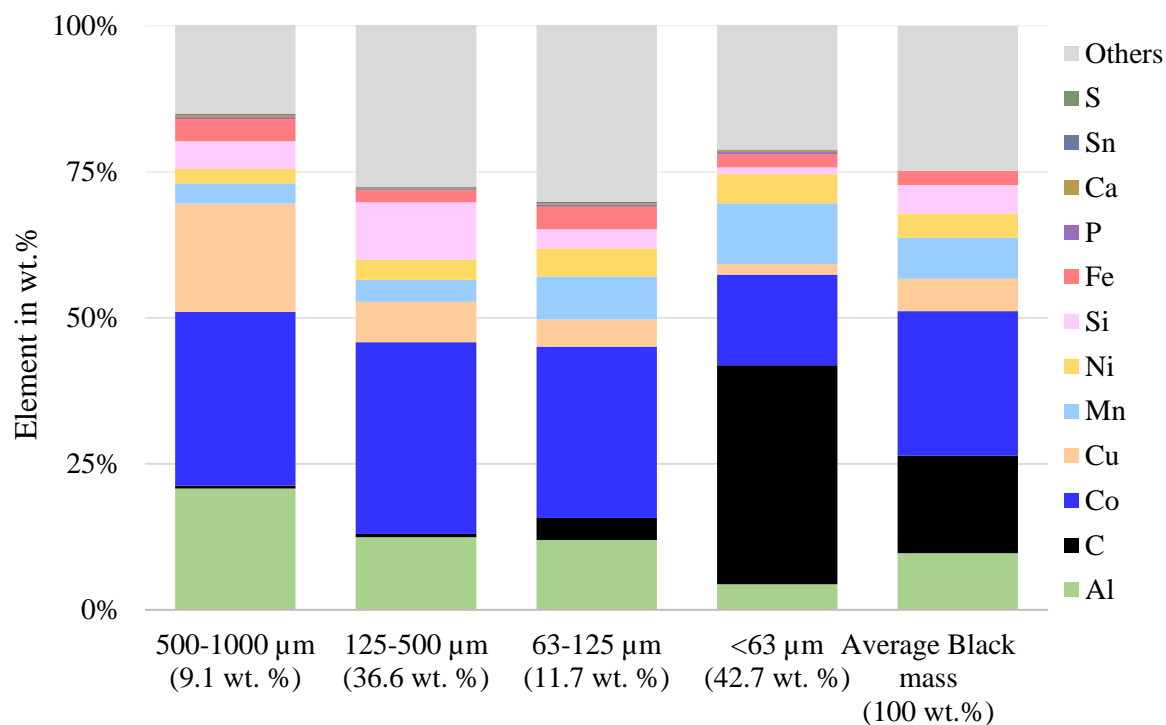


Figure 5 Bulk chemistry obtained by XRF and C analysis by LECO method.

In order to validate the results from automated mineralogy, it was necessary to compare the chemical composition calculated from the TIMA results to the bulk chemical composition XRF and C analysis for each analyzed sample (Figure 6). The chemical composition is calculated from the TIMA results according to the weight percentage of each phase in the sample and the chemical composition of corresponding phases, which was quantified from the EDX spectra. The 1:1 line is used to evaluate the agreement between these analytical methods and to provide a quality control. If there is a good agreement between the TIMA results and the bulk chemical composition, the points should fall on the 1:1 line. This would demonstrate that the phases and compositions defined when the reference list was compiled accurately describe the composition of the sample.

As seen in Figure 6, the points are closer to the line 1:1 as particle size decreases, which could be linked to the increasing uniformity of particle shape and size in fine size fractions. Automated mineralogy studies are associated with an inherent stereological bias as a result of the method being limited to two dimensions, but providing data which are used to describe three dimensional sample characteristics (Leißner et al., 2016; Pereira et al., 2020; Ueda et al., 2016). This stereological effect can help to explain the higher deviation from the 1:1 line for increasing particle size. The fraction below 63 μm mainly consists of active particles which are relatively round with similar sizes. In comparison, the particles in the coarse fractions are more anisotropic, with highly variable particle shapes. In the 500 – 1000 μm size fraction, Al and Cu are under-estimated by around 20 wt.% and 12 wt.% respectively, as is Al in the size fraction 63 – 125 μm . This is most probably related to the stereological effect since the Cu- and Al-bearing particles are anisotropic in shape, with the foil particles having a sheet-like morphology. Moreover, during the polishing of the grain mounts, the Al foil particles are challenging to polish and

may be removed from the surface as a result, which could contribute to the under-estimation of Al. In addition, the active particles can also be removed or detached from the Al foils during the polishing.

Errors can also be introduced to automated mineralogy studies by the sample preparation of grain mounts. Heinig *et al.* (2015) investigated the possible gravitational and shape related settling during sample preparation, and reported that coarse particles settle faster than fine particles and that round particles are likely to sink faster than sheeted particles with similar densities. The black mass particles are highly heterogeneous, in terms of size, shape and density, as previously mentioned. Therefore, the classification of the black mass in at least 4 size fractions helped to reduce the effects of gravitational separation due to size. However, when preparing grain mounts with coarser particle size distribution, fewer particles can fit into the grain mount in comparison to the fine fractions. The lower number of analyzed particles in the coarser fraction likely contributes to a higher deviation from the line 1:1 (Figure 6) (Mariano and Evans, 2015). As a consequence, at least two grain mounts for the fraction 500 – 1000 μm would be recommended to increase the number of analyzed particles. It is important to have enough particles to obtain

This study reveals the importance of sample preparation for black mass to reduce stereological bias and the need to have sufficient amount of particles to analyze in the coarser size fraction. Nevertheless, considering the challenges of analyzing such heterogeneous material and that the analyses required to first reference list for spent LIBs to be created and used, the results were highly positive. This correlation is satisfactory to justify the quantitative nature of automated mineralogy results.

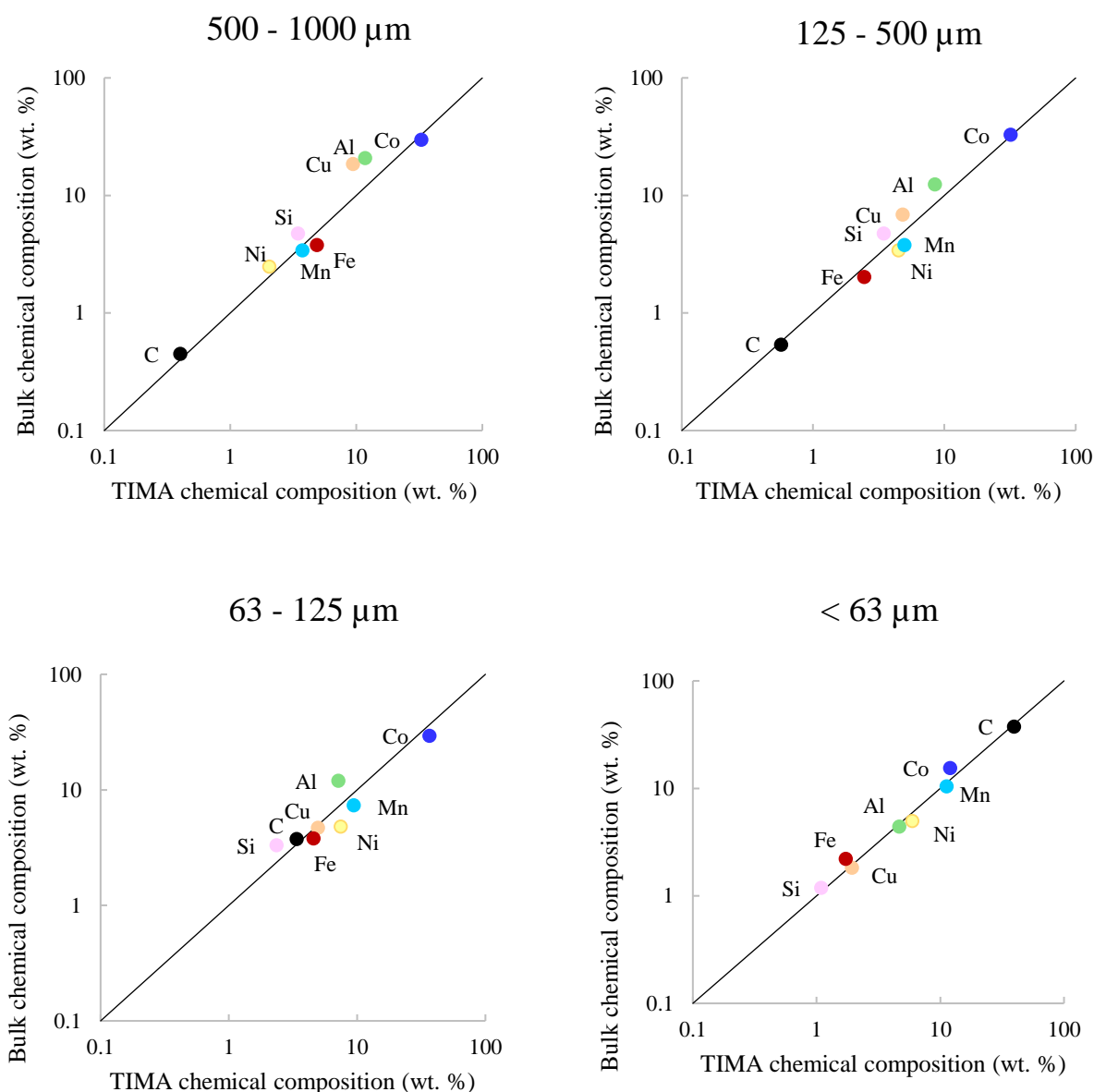


Figure 6 Comparison of the chemical composition calculated from automated mineralogy results vs. bulk chemical composition for the 4 characterized samples (500-1000 μm , 125-500 μm , 63-125 μm and < 63 μm). For a linear relationship, all elements should plot on the black line (1:1)

3.2. Identification of LIB components

The studied black mass exhibits a diverse range of particles containing the element Al. The main types of particles are Al foils, alloys and reaction products from pyrolysis, which are illustrated in Figure 7. The cathode chemistry LiNiCoAlO_2 is not expected to be present in this black mass and no lithium metal oxide particles were found with such chemistry.

The Al foil particles, such as particle A and B in Figure 7, are made of metallic and oxidized phases of Al. The metallic Al phase is usually surrounded by AlO phases in Al foil particles. Notably, the oxidation of Al and Cu electrode foils can occur during the operational lifetime of the battery as well as during recycling processes, such as pyrolysis. The corrosion of the foil is triggered by the electrochemical oxidation of solvent molecules and residual water in the electrolyte (Braithwaite et al., 1999; Ma et al., 2017; Theivaprakasam et al., 2018). During recycling processes, the electrolyte LiFP_6 decomposes to

form HF gas, which is highly corrosive and can react with the foils (Dai et al., 2017; Li et al., 2019; Lombardo, 2019). As a result, all black masses will likely contain foils with metallic and oxidized phases, the ratio of which is influenced by the lifetime of the battery and the type of recycling process.

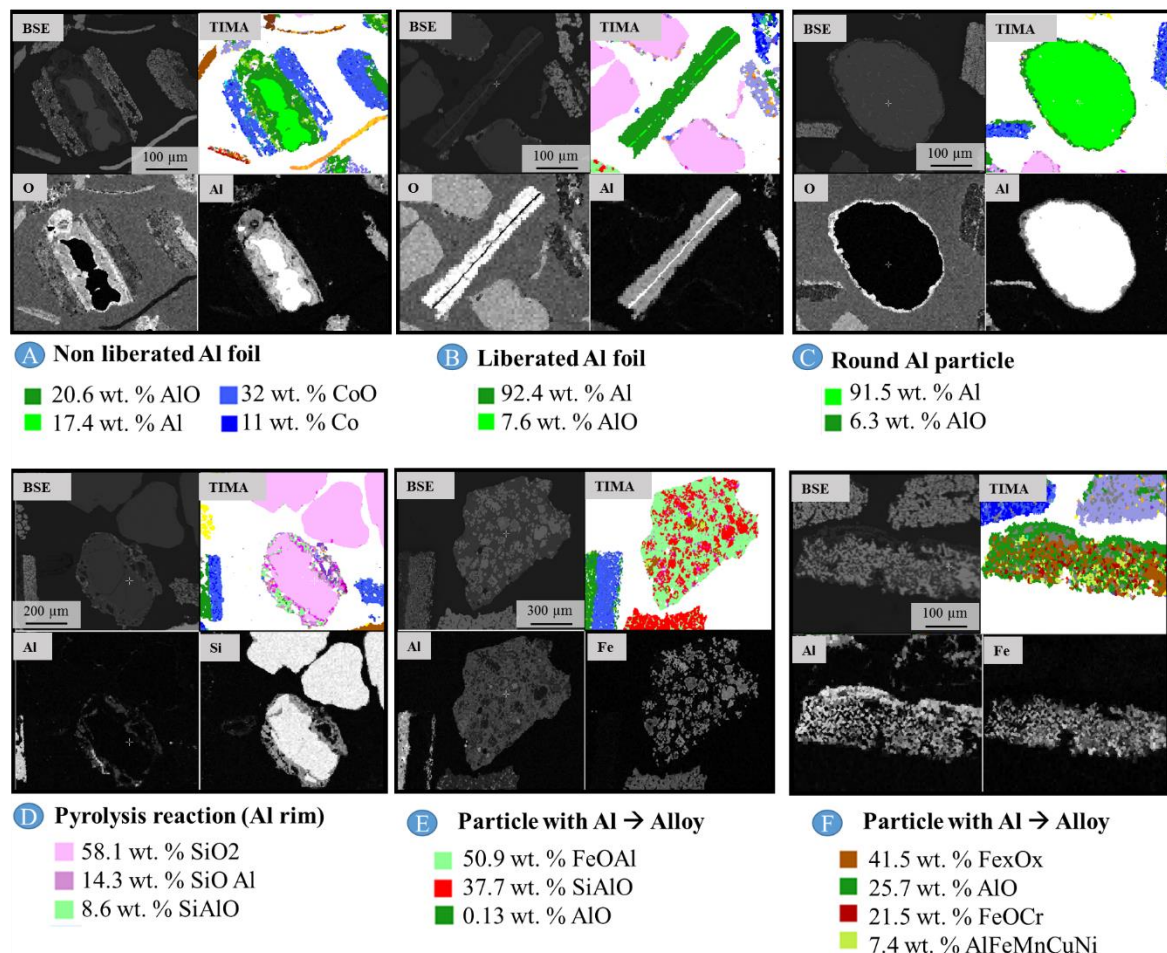


Figure 7 Different morphologies of particles containing Al and their main phases. A: Non liberated cathode with LCO, B: Liberated Al foil, C: round particles of Al, D: Reaction rim containing Al around Si particles, E: Alloy particle containing Al, F: BSE image with high resolution of an alloy particle. Top images: BSE image and TIMA: processed image; bottom images: elemental maps.

As observed in particles A and B in Figure 7, the Al foils appears to have rectangular shapes, fitting to the expected layer shape of the foils. However, the black mass also contains round particles of Al and AlO phases, such as particle C in Figure 7. As previously mentioned, the pyrolysis was conducted between 550 and 650 °C, values close to the melting point of Al (i.e. 630°C) (Fabian et al., 1997). It is highly likely that these round particles are Al droplets and testify to the partial melting of the Al foils during the pyrolysis stage. A second melting pattern is observed with the Si particles in the black mass, which were used as a filler for battery safety handling. Some of these Si particles present a partial rim principally containing Al and Si, such as particle D in Figure 7. This can be interpreted as a reaction product from the pyrolysis.

More complex particles, containing Al and other elements, including Fe, Mn, Cr, Cu, and Si, are present in the black mass, such as the particles E and F in Figure 7, and in Figure 8. According to Herrmann (2014), LIB casing is typically made of Al alloy or stainless steel. In the studied black mass, it cannot be assumed that these alloys are only the result of contamination from the crusher, and therefore, they must also partly originate from LIB casings. Alloy particles were identified in the studied black mass, with fragments of Fe/Mn in a Si/Al matrix (Figure 8).

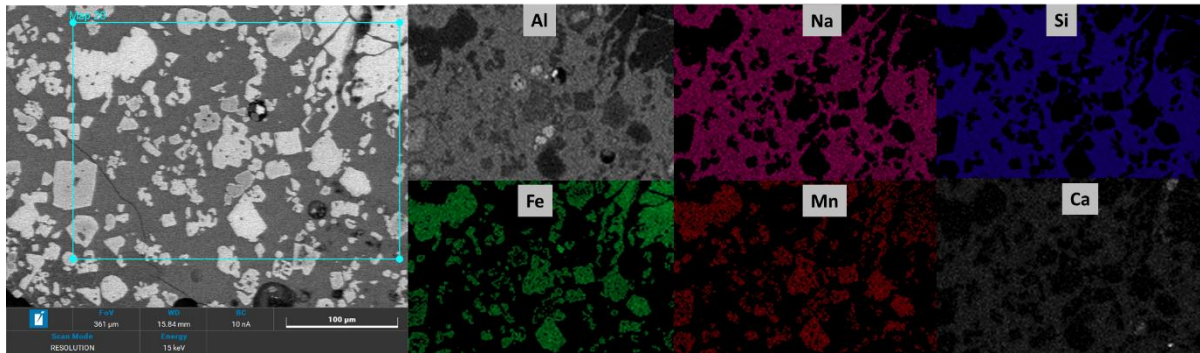


Figure 8 Elemental mapping of an alloy particle present in the studied black mass, showing the association of Al, Fe, Si and Mn.

With automated mineralogy, the MnO phase was identified in two types of LIB components, alloys and lithium metal oxides particles (NMC type). Therefore, it was important not to count the MnO from the alloy particles as lithium metal oxides, which would over-estimate the content of NMC. For this, a categorizer was applied to the particles containing the MnO phase as follows: if the particle contained MnNiCo-bearing and/or Co-bearing phases, then the particle is classified as NMC. Moreover, this categorizer allowed the distinction between LCO and NMC, as shown in Figure 9. With this method, the proportion of lithium metal oxides was estimated. Accordingly, the anode chemistry in this black mass contains 66.4% LCO and 33.6% NMC. Most of the current recycling processes are selective for one battery chemistry type, however a significant number of processes under development aim to handle cathode chemistry mixtures (Barik et al., 2017; Li et al., 2018; Zheng et al., 2018; Zou et al., 2013). This characterization technique successfully identified the NMC and LCO battery chemistries, and would also be able to detect NCA, LMO and LFP chemistries. Such information on the black mass composition is valuable to determine optimum black mass processing conditions.

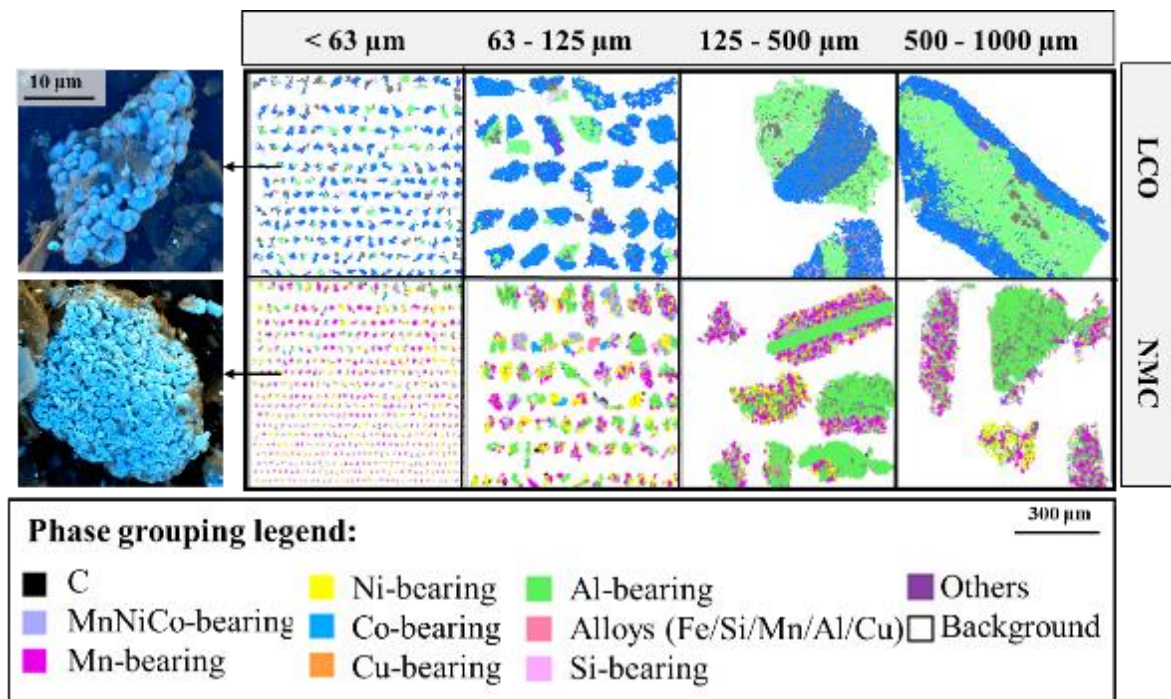


Figure 9 Example of the lithium metal oxides categorizer with LCO and NMC categories, applied to the different size fractions samples (not all the particles visible, sorted by size)

The anode components comprise two elements, Cu and C, which made the spectra collection and the particles identification relatively straightforward. The Cu foils are easily recognizable since the particles have a bright BSE level and are made of Cu and CuO phases. No melting pattern of Cu foils were

observed, in contrast to the Al foils. The melting point of Cu is 1085°C (Ma et al., 2018), which is much higher than the temperature at which the pyrolysis was conducted.

The carbon particles were well identified with automated mineralogy due to the use of iodized epoxy resin. However, the studied black mass contains different types of carbon particles, dominantly consisting of graphite particles, with nano-particles of carbon black and minor amounts of pyrolyzed coke particles. The nano-particles of carbon black were not detectable with this analytical tool which has a micrometer-scale resolution. However, Ross *et al.* (2020) reported that carbon black decomposes at around 500°C, and therefore it should not be present after the pyrolysis stage. If residuals of carbon black remain, they will not have a significant impact on the general carbon content. Moreover, during the pyrolysis stage, the organic materials, including the electrolyte, separator and binder from LIBs, were decomposed to lower molecular products such as pyrolysis oils, charcoal, water, and gas (Lombardo, 2019). Unfortunately it was not possible to distinguish between graphite and pyrolyzed coke with automated mineralogy, since they have the same EDX spectra.

To investigate the distribution of pyrolyzed coke particles in the samples, loose powder of the different size fractions of black mass samples were investigated with SEM. Out of the 4 fractions, pyrolyzed coke particles were only identified in the fraction below 63 µm. The morphology of the pyrolyzed coke particles is different from the graphite particles. As shown in Figure 10.A, they have relatively smooth surfaces with small pores and angular edges. The graphite particles, as shown in Figure 10.B, are more spherical, with lamella-like structures that correspond to the texture of the compacted graphite flakes. Only 5 particles out of more than 200 analyzed carbon particles were recognized as pyrolyzed coke, representing around 2 - 3% of the carbon particles population. Therefore, for the purposes of simplification, it was assumed that the pyrolyzed coke particle had a negligible impact on the analysis with automated mineralogy and that all the identified carbon particles were graphite particles.

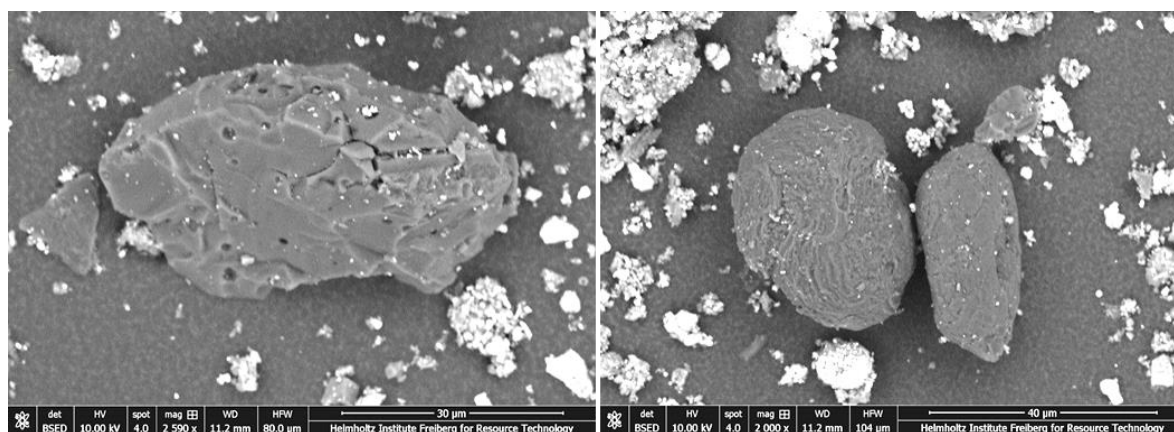


Figure 10 BSE images with SEM on loose powder samples from the < 63 µm fraction.
Righ 10.A: Probable pyrolyzed coke, left 10.B: two spheroidized graphite particles

3.3. Distribution of the LIB components

Based on the identification of the LIB components with automated mineralogy, their distribution in the black mass can be determined and is displayed in Figure 11. This black mass is composed of 17.5 wt.% graphite, 47.4 wt.% lithium metal oxides (NMC and LCO), 9.5 wt.% Al foils, 3.4 wt.% Cu foils, 15.2 wt.% of alloys. This study shows that black mass from spent LIBs produced by thermo-mechanical process can contain casing particles with different particle sizes. Most previous studies investigating LIB recycling have been conducted on black mass produced from manually dismantled electrodes rather than shredding of whole LIBs, and therefore these black masses did not contain casing particles (Liu et al., 2020; Wang et al., 2018; G. Zhang et al., 2018).

In addition, most of the research on black mass recycling uses elemental analysis to describe black mass samples. In those cases, the LIB components are linked to a specific dominant corresponding element, for instance Al to Al foils and Mn/Ni/Co to lithium metal oxides. However, as shown in this study if this approach is applied in studies with black mass from spent LIBs such as Pinegar and Smith (2019)

and Porvali *et al.* (2019), this could lead to an over-estimation of the Al foils and lithium metal oxides. Hence, when Fe or Cr is detected in the black mass, it could be a sign that the analyzed black mass contains alloy particles. Therefore, the presence of elements in more than one component demands caution for the interpretation of results based only on chemistry.

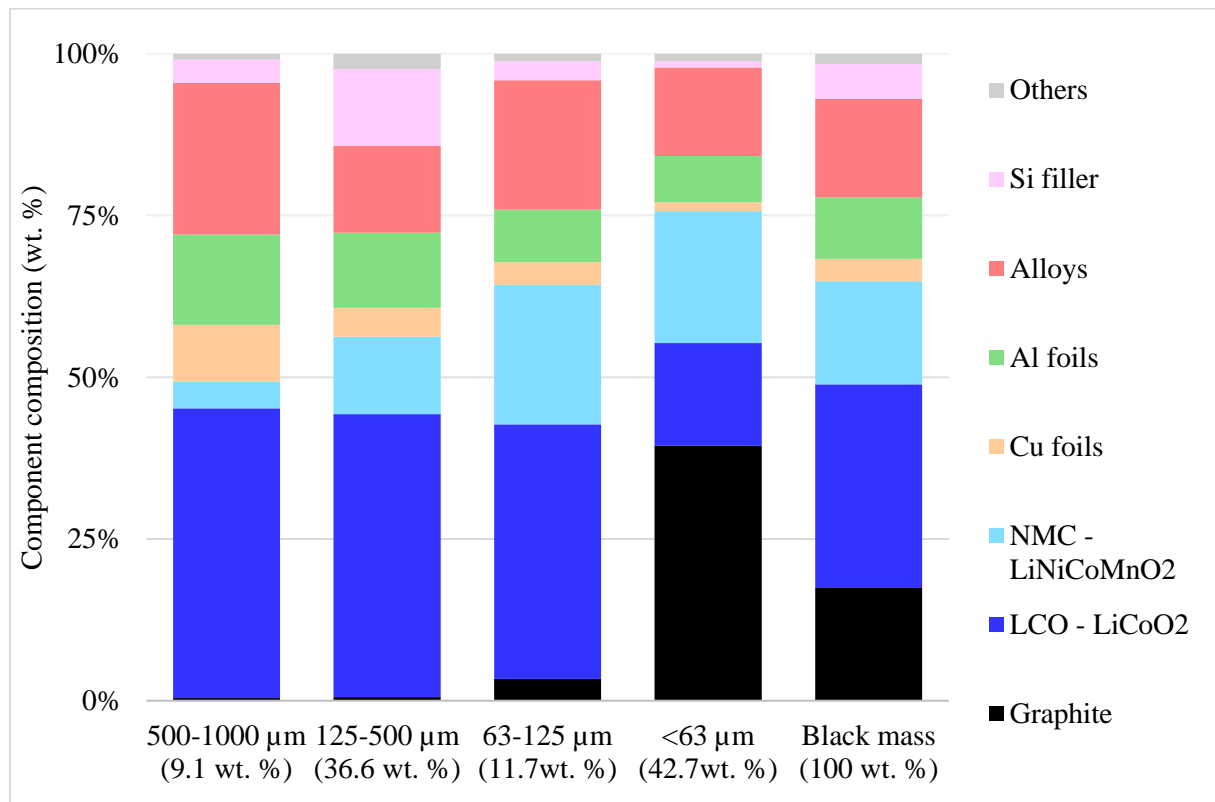


Figure 11 Content of LIB components in each size fraction of black mass. Lithium metal oxides types, NMC and LCO, were obtained with the categorizer.

Different concentration trends were observed in Figure 11 for the anode components and cathode components. The Al and Cu foil contents decrease with decreasing particle size. A similar trend was observed for the industrial black mass reported by Ruismäki *et al.* (2020), which was mechanically processed. However, the thermo-mechanical black mass of this study has a higher foil content in the fine fraction, particularly the Al foils with 7.3 wt.%, compared to the aforementioned mechanical black mass, which contains around 1 wt.% of Al in the fraction below 100 μm (Ruismäki *et al.*, 2020). This difference can be linked to the pyrolysis stage during the recycling process. Li *et al.* (2019), who studied the effect of vacuum pyrolysis on cathode electrode, confirmed that, as the temperature approaches the melting point of Al, the Al foil becomes more brittle. This brittle behavior creates more fine particles of Al foils during the following crushing stage.

The Cu foils were concentrated in the coarse fraction and the carbon particles were predominantly found in the fraction below 63 μm. For this thermo-mechanical black mass, a sieving process would be sufficient to separate Cu foils and graphite. In comparison, the cathode components, Al foils and lithium metal oxides, are distributed throughout the different size fractions, and a classification process would not be suitable for their separation. The lithium metal oxides have more or less the same distribution throughout the 500 – 1000 μm, 125 – 500 μm and 63 – 125 μm size fractions, with a content around 50 wt.%. These trends highlight a different liberation behavior for the anode and the cathode as a consequence of the chosen processing stages, which will be further elaborated in the following section.

3.4. Liberation of LIB components

LIBs are manufactured following a specific design, a succession of cells, each cell is made of a cathode and anode electrode, and these two electrodes are isolated by a separator. As explained in Figure 1, each electrode is made of a foil with coated particles, Al foil with lithium metal oxides and Cu foil with

graphite. Accounting for this design, if a Cu foil particle is in contact with lithium metal oxides, it can be deduced that this contact occurs during the recycling process because they should not be in direct contact in the battery cell. Therefore, in this study, two types of liberation of the components were calculated. A liberation from the design (A), for this calculation only the component from one electrode type were considered. For the anode components only the association between graphite and Cu foils were considered, for the cathode components only Al foils and Li-metal oxides, therefore the associations between electrode components types were not considered for the calculation (A). The second liberation analysis (B) takes the effects of the recycling process into account, as well as the liberation from the design. For the calculation of the latter, all the LIB components were considered, Cu foils or graphite in contact with lithium metal oxides or Al foils. The results are presented in Table 4. Moreover, to better understand the decrease of liberation degree from (A) to (B), the locking analysis and free surface of the LIB components are displayed in Figure 12.

Table 4 Liberation degree of LIB components obtained with the liberation categorizer.
(A) Design liberation and (B) Recycling process liberation. (*) fraction affected by touching particles

LIB components	500-1000 μm (9.1 wt.%)		125-500 μm (36.6 wt.%)		63-125 μm (11.7 wt.%)		< 63 μm * (42.7 wt.%)		Black mass (100 wt.%)	
	A	B	A	B	A	B	A	B	A	B
Context of liberation										
Al foils	18.3	17.2	17.0	16.4	36.1	32.9	62.8	60.2	33.4	31.8
Cu foils	60.2	58.2	62.2	57.9	57.9	53.4	59.1	50.9	59.3	54.7
Lithium metal oxides	2.9	2.8	7.4	7.1	42.8	41.1	86.7	79.7	39.4	37.4
Graphite	19.8	12.5	25.3	19.5	58.4	44.5	91.2	76.8	89.7	75.3

In general, the liberation degree of all the components tends to increase with decreasing particle size (Table 4). It is important to highlight that the liberation degree of the components in the fraction < 63 μm is under-estimated due to particles touching each other. Touching particles is a well-known challenge in automated mineralogy and affects the liberation analysis (Poliakov and Donskoi, 2019; Røisi and Aasly, 2018). For this study, graphite filler could not be used during sample preparation, as recommended by Røisi *et al.* (2018). The touching-particles function from TIMA worked well to separate touching particles for the samples 500 – 1000 μm , 125 – 500 μm and 63- 125 μm . However, the fraction below 63 μm remained challenging, due to the high number of particles and particle agglomeration. In particular, the graphite liberation degree (B) was affected, decreasing from 91.2% to 76.8%, due to its contact with fine particles of lithium metal oxides, as at least 5% of the graphite is locked with lithium metal oxides (Figure 12). It is worth pointing out that, based on the battery cell design, graphite and lithium metal oxides are not supposed to be in contact. Moreover, SEM analysis on dry lose powder showed that the graphite particles in the fraction below 63 μm are liberated (e.g. Figure 10) and not agglomerated with lithium metal oxides. Thus, the agglomeration phenomena likely happened when the powder was mixed with liquid resin during sample preparation, and brings an undesired bias to the analysis. Since this study also aimed to identify limitations of the applied methods, in order to develop suitable characterization methodologies, it can be recommended that the component-level liberation (A) for the graphite and lithium metal oxides should be used.

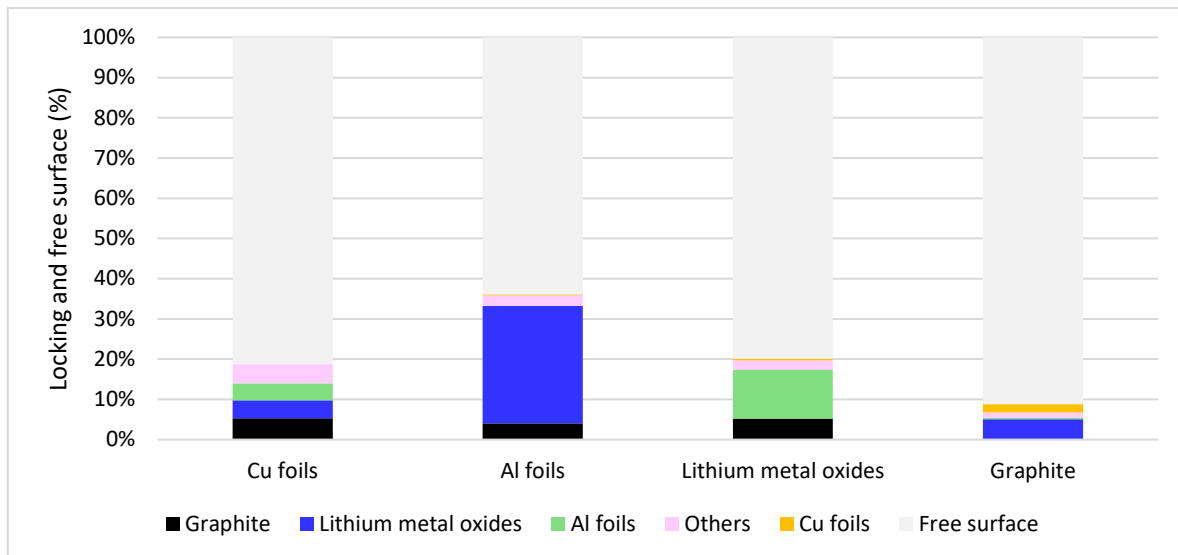


Figure 12 Locking and free surface of LIB components for the whole black mass

As shown in Table 4, the anode components, Cu foils and graphite particles, display a better liberation than the cathode components, Al foils and lithium metal oxides. Only 33.4% of the Al foil are liberated, and the liberation degree increases with finer particles sizes. The difference between the two liberation analyses is minor, 33.4% for (A) and 31.8% for (B). The non-liberated Al foils have a free surface of 64% and are mainly locked in association with lithium metal oxides, 29.2% (Figure 12). These particles often preserved the laminated structure of the cathode electrode from the battery manufacturing, such as particle “A” in Figure 7, with the Al foil surrounded by lithium metal oxides on both sides, which explains the low free surface for this component.

The lack of liberation of the Al foil in this case can be associated with the presence of residual binder, which maintains the adhesion between foils and the active particles. A content of 1.7 wt.% F was measured in the 500 – 1000 μm fraction and 2.1 wt.% in the 125 – 500 μm fraction. This clearly demonstrates that, even with a pyrolysis at 600 $^{\circ}\text{C}$ of non-crushed spent LIBs, not all binder is decomposed. The studies from Sun *et al.* (2011) and Li *et al.* (2019) reported that 600 $^{\circ}\text{C}$ is the optimal temperature for vacuum pyrolysis in order to remove the lithium metal oxides coated on the Al foil. However the pyrolysis in these studies was conducted on manually dismantled electrodes whereas in the present research the battery were directly pyrolyzed, so the electrodes were all packed together. The compacted structure of the electrodes in the battery may influence the pyrolysis process because the electrode surfaces are not directly exposed, reducing the decomposition of the binder.

Compared to Al foils, the Cu foils presented a higher free surface of more than 80% (Figure 12). This difference of liberation between anode and cathode foils may be due to binder type and its interaction with the active particles. PVDF is commonly used in anodes and cathodes, however being environmental un-friendly, efforts to replace PVDF by water soluble binders are ongoing (i.e. SBR-CMC) (Bresser *et al.*, 2018; Versaci *et al.*, 2017; Yen *et al.*, 2013). Zhang *et al.* (2019b) showed that SBR is decomposed at 450 $^{\circ}\text{C}$, and therefore would have been decomposed during the conducted pyrolysis stage, unlike PVDF, as previously mentioned. In addition, it was shown by Widijatmoko *et al.* (2020) that the interaction between graphite and PVDF is weaker than between lithium metal oxides and PVDF. The latter would explain why the Cu foils are better liberated from the graphite particles than the Al foils from the lithium metal oxides.

As shown in Figure 12, the locking analysis of the Cu foils yields a higher diversity in associated components compared with Al foils. Cu foils are not only locked with graphite particles, but also with Al foils, lithium metal oxides and others. This result explains the different values of liberation calculation for the Cu foil, 59.3% for (A) and 54.7% for (B). The Cu foils have a ductile behavior (Or *et al.*, 2020) and can be folded, which can lead to a lower liberation by causing the entrapment of other components in the folds, such as “B”, “D” and “E” in Figure 13. For instance in particle “D”, the Cu foil appears to have wrapped around graphite particles during the crushing process, protecting them

from impact and shearing processes during the crushing stage. Therefore, the lack of liberation of Cu foils is not linked with the binder, as with the cathode, but with its ductile behavior during the crushing stage.

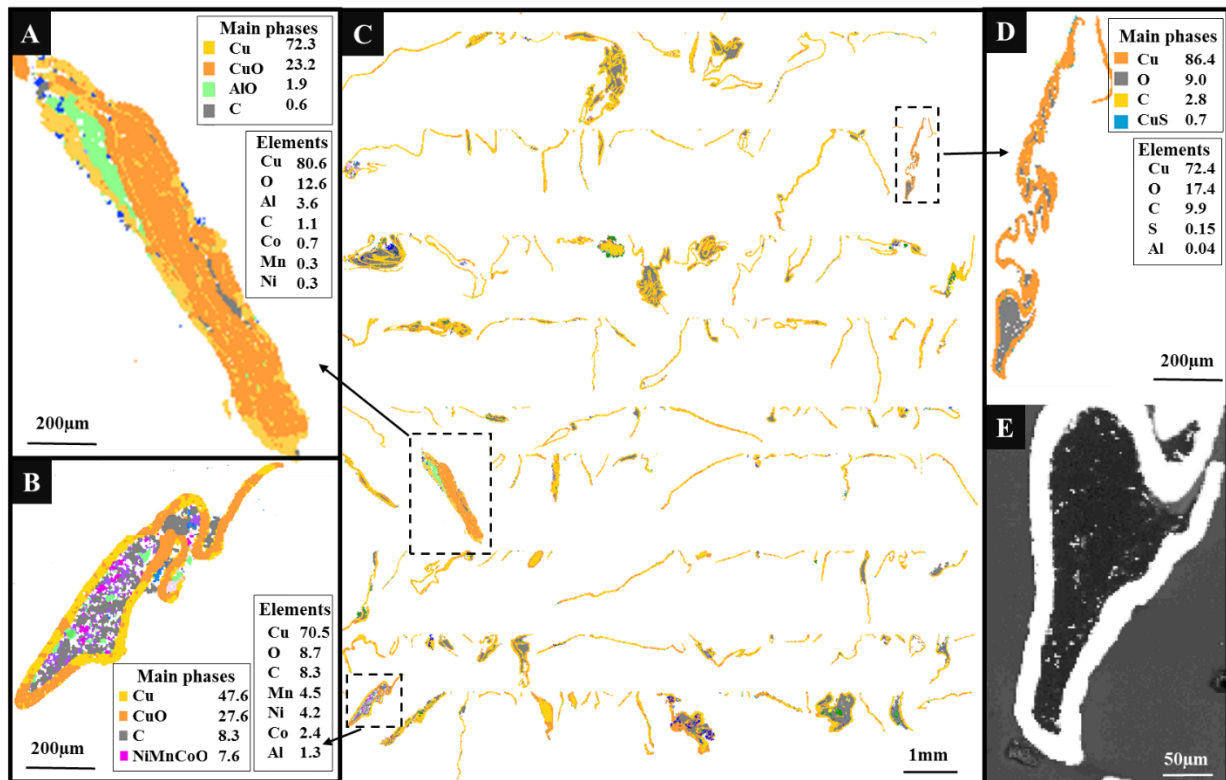


Figure 13 Various Cu foil particles. A: AlO locked inside Cu foils and surrounded by a few lithium metal oxides. B: particles locked inside Cu foils. C: Particles sorted by Cu content. D: SEM of non-liberated Cu foil with C particles. E: BSE image of non-liberated graphite

The size distribution of the LIB components in the black mass was determined with automated mineralogy using the equivalent circle diameter. This method underestimates the length of elongated particles and is therefore not optimal in such cases. A new function is been developed for TIMA software, which measures the mean intercept length in the 4 directions of the particles, this function would be more appropriate for elongated particles. The size distribution displayed in Figure 14 is obtained by combining the results from the four size fractions. Most of the non-liberated particles had a size over 50 μm and the liberated particles below 50 μm . The results indicate that this process yielded sufficient liberation with respect to the graphite particles. A D_{80} of 24 μm was measured for liberated graphite particles, which is consistent with the diameter of a spheroidized graphite particle of 20 – 30 μm (Frey, 2018; Li and Sun, 2016). This result implies that most of the liberated graphite particles are found as single particles, as 96 wt.% of the C occurs in the fraction below 63 μm .

For this study, a particle composed of only one LIB component is categorized as liberated. The liberated metal oxides have a D_{80} of 76.2 μm and present a bimodal distribution in Figure 14, with one population around 15 μm and a second one around 96 μm . However, the pristine lithium metal oxides particles have a D_{80} of ca. 25 μm before the calendaring process in battery manufacturing, which is smaller than the measured D_{80} of this thermo-mechanical black mass (Pavoni et al., 2018; Tsai et al., 2018; Yudha et al., 2019). This result can be explained by the conservation of the aggregate morphology from the battery manufacturing. This aggregation might be due to the existence of residual binder after pyrolysis, both within the aggregates and also on their surfaces (c.f. dark layer on the LCO particle SEM false color image Figure 9).

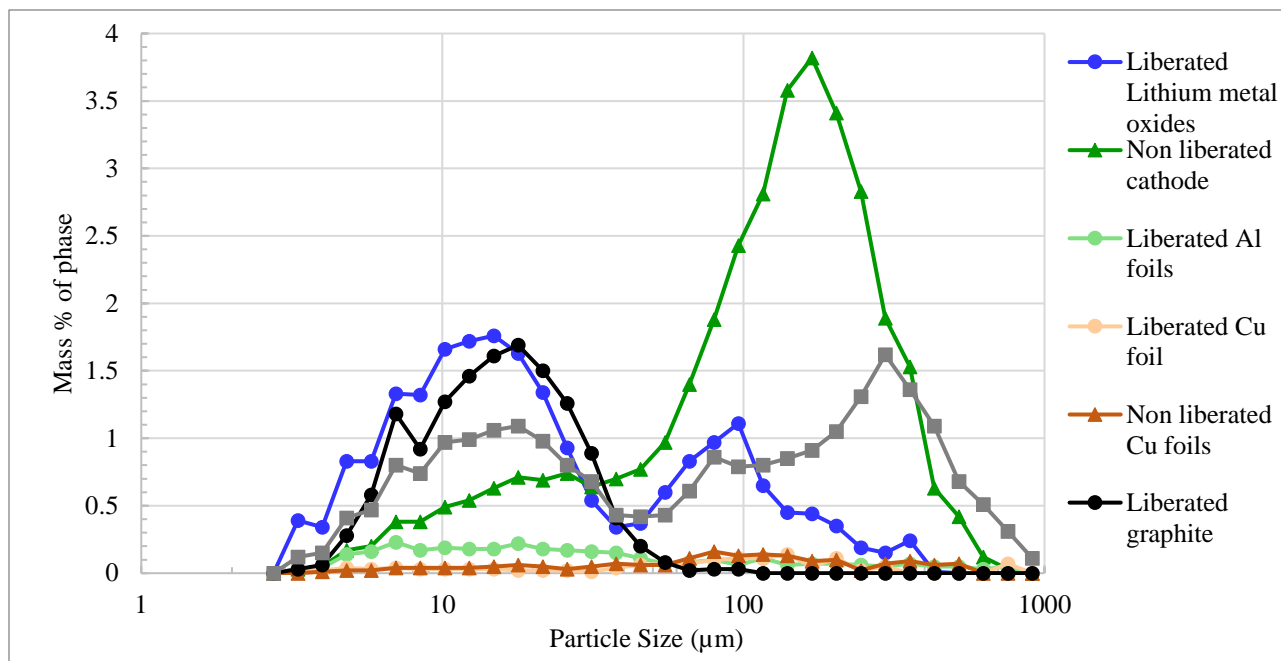


Figure 14 Size (equivalent circle diameter) distribution of the liberated and non-liberated LIB components

4. Conclusions

This study illustrates the applicability of automated mineralogy to the characterization of an industrial black mass obtained from spent LIB waste after pyrolysis, crushing and sieving. This novel characterization approach provides quantitative data for each individual particle of the entire particle population, including sizes, shapes and composition. For complex secondary materials like black mass, this method enables the acquisition of detailed information on the phases present, which can be seen as “anthropogenic minerals”. The characterization of this secondary material by other means is challenging, as many elements can be present in more than one LIB component. Therefore, categorizer scripts were implemented to distinguish between different LIB components: Al foils, Cu foils, casing, graphite and lithium metal oxides. Moreover, real mixed battery waste contains more than one lithium metal oxide chemistry, so a categorizer was developed to differentiate lithium metal oxides, in this case NMC and LCO. With this method, it was possible to identify and quantify the different LIB components present in the black mass. Both the reference list and the categorizers developed in this study could be applied to other black mass samples from LIB recycling, and even other similar materials with some modifications.

The wealth of information obtained by automated mineralogy can help to improve the efficiency of the particulate recycling processes, i.e. size reduction and separation, including thermal treatments such as pyrolysis. The main findings and conclusions of this article can be summarized as follows:

- A black mass contains cell components such as Al foils, Cu foils, lithium metal oxides and graphite. However, it can also contain metal alloy particles with diverse particles sizes, not only in the fraction over 1 mm. These alloys mainly comprise Fe and Si, but also Al, Mn or Ni.
- Selective liberation of the Cu foils was achieved, in contrast to the Al foil (i.e. 54.7% vis-à-vis 31.8%), which is assumed to be linked to the presence of residual PVDF binder on the surface of the lithium metal oxides and the Al foil. The non-liberated Al foil often preserved the lamination of cathode manufacturing (lithium metal oxides on both or one side of the Al foil). The lithium metal oxides liberated from the Al foils can retain the aggregated morphology from manufacturing, resulting in a bimodal distribution of the liberated lithium metal oxides.
- Pyrolysis increased the corrosion (oxidation) of the Al foils and led to brittle behavior, which created fine particles during crushing and resulted in the contamination of the finer fractions of the black mass.
- The Cu foils were well liberated, i.e. mechanically delaminated. However, their ductile nature led to entrapment of graphite particles and other fine particles, although not to a large extent.

- Graphite particles were individually liberated and 96 wt.% were concentrated in the fine fraction, < 63 μm .

In summary, an approach for the characterization of complex and fine particles of a secondary material stream has been successfully developed. This is particularly useful for mechanical recycling, as shown by the application to a case study of the black mass fraction of spent LIBs. The methodology proposed will be further used to quantify the efficiency of different recycling processing routes (mechanical, thermo-mechanical and electrohydraulic fragmentation) especially with regards to liberation and particle properties which promote separation.

Acknowledgements and funding

The authors would like to acknowledge: Marek Dosbaba for the possibility to work with TESCAN; Accurec GmbH for providing the black mass, UVR FIA GmbH for the XRF analysis; From Helmholtz Institute Freiberg: Roland Wuerkert, Michael Stoll and Sebastian Thormeier for the grain mounts preparation; Robert Moeckel and Doreen Ebert for their help with the analytical work. The authors gratefully acknowledge the Helmholtz foundation for base funding within the PoF III (project oriented funding part III) for the BooMeRanG project.

Author Contributions

Conceptualization, writing and data curation, A.V; Resources, investigation and software teaching, E.G; reviewing and editing, R.B and K.B; reviewing and supervision, M.R and R.S.G. All authors have read and agreed to the published version of the manuscript.

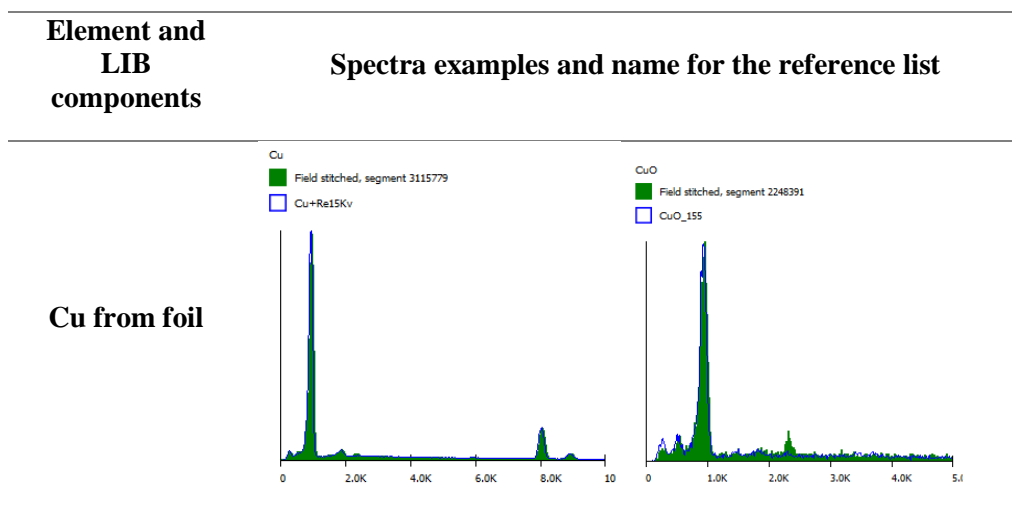
Declaration of Competing Interest

The authors declare that they have no known competing financial interests or personal relationships that could have appeared to influence the work reported in this paper.

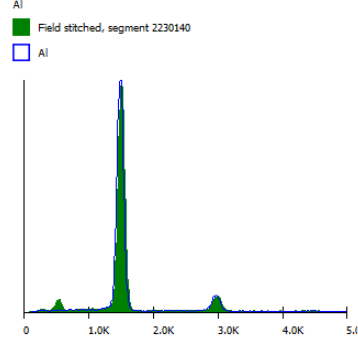
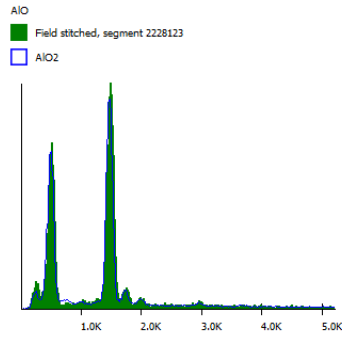
Supplementary materials

Supplementary S1: Examples of collected spectra on distinguishable LIB component to build the reference list. S2: Compositional thresholds of the collected spectra for the reference list.

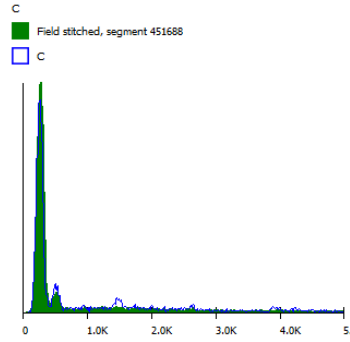
Supplementary material S1: Examples of collected spectra on distinguishable LIB component to build the reference list (blue spectra). On the left, extracted examples of spectra: in green the specific measured spectra and in blue the closest match from the created reference list.



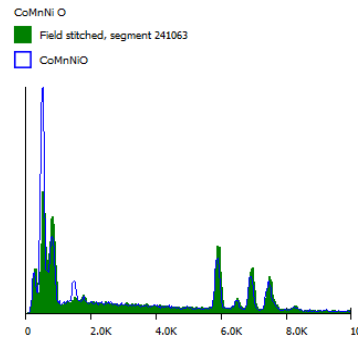
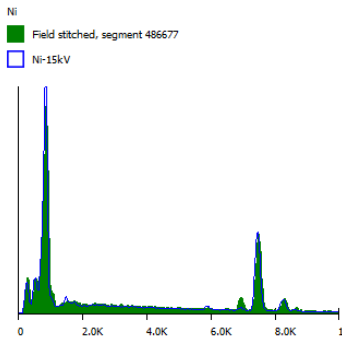
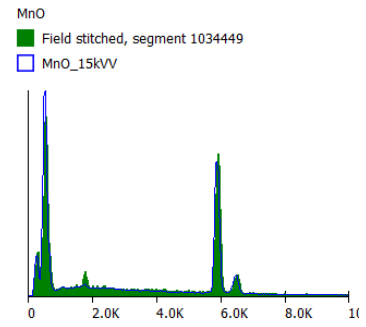
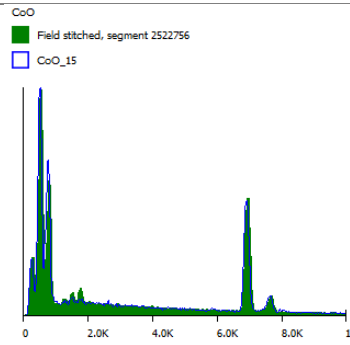
Al from foil

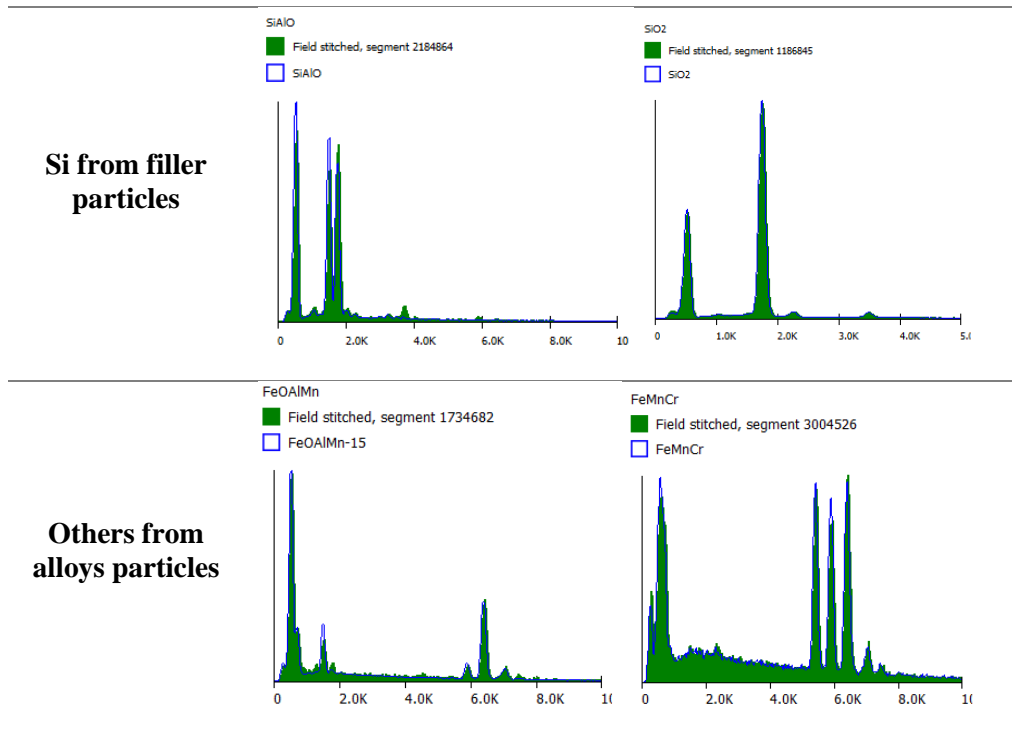


C from graphite



**Metals from
lithium metal
oxides:
Co, Ni, Mn
and mix**





Supplementary material S2 - Compositional thresholds of the collected spectra. (Phase name: the main elements by decreasing content)

Category	Phase name	Composition (%)
Cu-bearing	Cu	Cu 100
	CuO	Cu 79.89, O 20.11
	CuS	79.85, S 20.15
Al-bearing	Al	Al 100
	AlO	Al 88.51, O 11.49
C	C	C 100
Co-bearing	Co	Co 100
	CoO	Co 76.43, O 23.57
	CoClO	Co 51.35, O 32.53, Cl 16.12
	CoAlO	Co 74.84, O 19.65, Al 5.51
Ni-bearing	Ni	Ni 100
Mn-bearing	MnO	Mn 77.52, O 22.48
NiMnCo-bearing	NiCoO	Ni 53.10, O 34.53, Co 10.07, Al 2.30
	NiMnCoO	Ni 39.73, Mn 27.18, Co 19.21, O 11.62, Al 2.25

	MnCoNiO	Mn 36.11, Co 25.53, Ni 19.93, O 15.44, Al 2.99
	CoMnNiAlO	Co 26.07, O 25.99, Mn 22.79, Ni 22.60, Al 2.55
	NiCoMnO+CeLa	Ni 40.78, Ce 18.05, Co 13.17, La 10.66, O 8.02, Mn 7.40, Al 1.92
	NiCoMnO+CeLa2	Ni 36.61, Ce 16.18, La 15.87, O 11.90, Co 9.96, Mn 6.12, Al 2.01, Si 1.33
Si-bearing	Si	Si 100
	SiOx	O 53.26, Si 46.74
	SiAlO	O 54.27, Si 41.24, Al 4.49
	SiAlO2	O 53.92, Si 23.24, Al 22.84
Alloys	CrAlMnO	Cr 47.52, O 31.62, Al 12.91, Mn 7.95
	Fe	Fe 100
	FeOx	Fe 75.92, O 24.08
	FeMnAlO	Fe 55.23, O 27.89, Mn 8.60, Al 8.29
	FeMnO	Fe 43.66, Mn 28.85, Cr 27.49
	FeMnCr	Fe 43.66, Mn 28.85, Cr 27.49
	FeCuSO	Fe 33.19, Cu 32.45, S 22.62, O 10.73, Si 1.01
	FePCu	Fe 36.60, O 35.40, P 16.81, Cu 8.35, Ca 2.84
	FeNi	Fe 58.79, Ni 41.21
	FeNiO	Fe 45.98, O 26.54, Ni 21.67, Ca 2.23, Si 1.91, Al 1.67
	FeTiO	Fe 35.48, O 31.74, Ti 29.28, Si 2.14, Al 1.36
	AlFe	Al 80.00, Fe 20.00
	AlFeMnCuNiO	O 30.87, Al 18.91, Fe 15.93, Mn 13.97, Cu 7.29, Ni 4.68, Co 2.94, P 2.24, Mg 1.58, Cr 1.58
	MnFeAlCrO	O 31.84, Mn 26.31, Fe 20.56, Al 14.79, Cr 4.06, Mg 2.48
	MnAlFeCrO	O 36.89, Mn 29.90, Al 14.35, Fe 7.15, Cr 3.62, Ca 2.36, P 2.16, Si 2.05, Mg 1.54
	FeCuMnCrNiAlO	Fe 39.77, O 23.69, Cu 10.10, Mn 10.05, Cr 5.93, Ni 5.07, Al 3.58, Si 1.80
	FeCuSO	Fe 33.19, Cu 32.45, S 22.62, O 10.73, Si 1.01
	Sn	Sn 100
SnNiFeO	Sn 52.68, Ni 37.22, O 5.08, Fe 4.02	

	SnCuFeCa	Sn 63.27, O 21.32, Cu 8.55, Fe 5.76, Ca 1.10
	CuSn	Cu 54.32, Sn 45.68
	CuAlOS	Cu 53.29, O 25.27, Al 13.59, S 7.85
	CuSnNiFeO	Cu 32.71, O 21.01, Sn 20.66, Ni 12.30, Fe 11.02, Si 1.50, Al 0.79
	ZrMnNiCrTiO	Zr 31.82, O 26.59, Mn 12.63, Ni 11.38, Cr 8.39, Ti 7.94, K 1.25
	SiMgAlO	O 60.78, Si 18.46, Mg 15.21, Al 5.55
Other	CaSO	O 41.20, Ca 32.81, S 25.99
	CaSiO	O 48.21, Ca 45.94, Si 5.85
	CaCO	O 47.96, Ca 40.04, C 12.00
	CaOP	Ca 39.36, O 38.76, P 18.25, Cl 2.32, F 1.24, H 0.07
	PFeO	O 67.20, P 31.62, Fe 1.17
	SiMgAlKO	O 50.47, Si 21.84, Mg 14.15, Al 9.16, K 4.37
	CaSiO	O 48.21, Ca 45.94, Si 5.85
	SiCaAlO	O 48.28, Si 25.37, Ca 18.45, Al 7.90

References

- Akimoto, J., Gotoh, Y., Oosawa, Y., 1998. Synthesis and Structure Refinement of LiCoO₂ Single Crystals. *J. Solid State Chem.* <https://doi.org/10.1006/jssc.1998.7966>
- Bachmann, K., Frenzel, M., Krause, J., Gutzmer, J., 2017. Advanced Identification and Quantification of In-Bearing Minerals by Scanning Electron Microscope-Based Image Analysis. *Microsc. Microanal.* 23, 527–537. <https://doi.org/10.1017/S1431927617000460>
- Barik, S.P., Prabaharan, G., Kumar, L., 2017. Leaching and separation of Co and Mn from electrode materials of spent lithium-ion batteries using hydrochloric acid: Laboratory and pilot scale study. *J. Clean. Prod.* 147, 37–43. <https://doi.org/10.1016/j.jclepro.2017.01.095>
- Blomgren, G.E., 2017. The Development and Future of Lithium Ion Batteries. *J. Electrochem. Soc.* 164, A5019–A5025. <https://doi.org/10.1149/2.0251701jes>
- Braithwaite, J.W., Gonzales, A., Nagasubramanian, G., Lucero, S.J., Peebles, D.E., Ohlhausen, J.A., Cieslak, W.R., 1999. Corrosion of Lithium-Ion Battery Current Collectors. *J. Electrochem. Soc.* 146, 448–456. <https://doi.org/10.1149/1.1391627>
- Bresser, D., Buchholz, D., Moretti, A., Varzi, A., Passerini, S., 2018. Alternative binders for sustainable electrochemical energy storage—the transition to aqueous electrode processing and bio-derived polymers. *Energy Environ. Sci.* 11, 3096–3127. <https://doi.org/10.1039/c8ee00640g>
- Buchmann, M., Schach, E., Tolosana-Delgado, R., Leibner, T., Astoveza, J., Kern, M., Möckel, R.,

- Ebert, D., Rudolph, M., van den Boogaart, K., Peuker, U., 2018. Evaluation of Magnetic Separation Efficiency on a Cassiterite-Bearing Skarn Ore by Means of Integrative SEM-Based Image and XRF–XRD Data Analysis. *Minerals* 8, 390. <https://doi.org/10.3390/min8090390>
- Chehreh Chelgani, S., Rudolph, M., Kratzsch, R., Sandmann, D., Gutzmer, J., 2016. A Review of Graphite Beneficiation Techniques. *Miner. Process. Extr. Metall. Rev.* 37, 58–68. <https://doi.org/10.1080/08827508.2015.1115992>
- Chen, M., Zheng, Z., Wang, Q., Zhang, Y., Ma, X., Shen, C., Xu, D., Liu, J., Liu, Y., Gionet, P., O'Connor, I., Pinnell, L., Wang, J., Gratz, E., Arsenault, R., Wang, Y., 2019. Closed Loop Recycling of Electric Vehicle Batteries to Enable Ultra-high Quality Cathode Powder. *Sci. Rep.* 9, 1–9. <https://doi.org/10.1038/s41598-018-38238-3>
- Cheng, E.J., Taylor, N.J., Wolfenstine, J., Sakamoto, J., 2017. Elastic properties of lithium cobalt oxide (LiCoO₂). *J. Asian Ceram. Soc.* 5, 113–117. <https://doi.org/10.1016/j.jascer.2017.03.001>
- Dai, S., Chen, Jian, Ren, Y., Liu, Z., Chen, Jianlin, Li, C., Zhang, Xinyuan, Zhang, Xiao, Zeng, T., 2017. Electrochemical Corrosion Behavior of the Copper Current Collector in the Electrolyte of Lithium-ion Batteries. *Int. J. Electrochem. Sci* 12, 10589–10598. <https://doi.org/10.20964/2017.11.28>
- Diekmann, J., Hanisch, C., Froböse, L., Schällicke, G., Loellhoeffel, T., Fölster, A.-S., Kwade, A., 2017. Ecological Recycling of Lithium-Ion Batteries from Electric Vehicles with Focus on Mechanical Processes. *J. Electrochem. Soc.* 164, A6184–A6191. <https://doi.org/10.1149/2.0271701jes>
- Evertz, M., Lürenbaum, C., Vortmann, B., Winter, M., Nowak, S., 2015. Development of a method for direct elemental analysis of lithium ion battery degradation products by means of total reflection X-ray fluorescence. *Spectrochim. Acta - Part B At. Spectrosc.* 112, 34–39. <https://doi.org/10.1016/j.sab.2015.08.005>
- Fabian, H., Richardson, H., Habashi, F., Besold, R., 1997. Volume II: Primary Metals, Secondary Metals. *Light Metals. Handb. Extr. Metall.* by F. Habashi, 581-640. Weinheim Wiley VCH.
- Fandrich, R., Gu, Y., Burrows, D., Moeller, K., 2007. Modern SEM-based mineral liberation analysis. *Int. J. Miner. Process.* 84, 310–320. <https://doi.org/10.1016/j.minpro.2006.07.018>
- Frey, C., 2018. Processing of natural flake graphite for Lithium-Ion-Batteries, in: *Proceedings of EMPRC 2018*. pp. 203–210.
- Gottlieb, P., 2008. The Revolutionary Impact of Automated Mineralogy on Mining and Mineral Processing, in: *Conference: XXIV International Mineral Processing Congress At: Beijing, China* Volume: *Proceedings of XXIV IMPC*.
- Gu, F., Guo, J., Yao, X., Summers, P.A., Widijatmoko, S.D., Hall, P., 2017. An investigation of the current status of recycling spent lithium-ion batteries from consumer electronics in China. *J. Clean. Prod.* 161, 765–780. <https://doi.org/10.1016/j.jclepro.2017.05.181>
- Gu, Y., 2003. Automated Scanning Electron Microscope Based Mineral Liberation Analysis An Introduction to JKMRC/FEI Mineral Liberation Analyser. *J. Miner. Mater. Charact. Eng.* 02, 33–41. <https://doi.org/10.4236/jmmce.2003.21003>
- Gy, P., 1994. Sampling—diving into the unknown. *LC-GC*. LC-GC 12(11)808–.
- Heinig, T., Bachmann, K., Tolosana Delgado, R., Van den Boogaart, K., Gutzmer, J., 2015. Monitoring gravitational and particle shape settling effects on MLA sample preparation, in: *IAMG Conference*.
- Herrmann, M., 2014. Packaging-Materials review, in: *AIP Conference Proceedings* 1597, 121. pp. 0–14. <https://doi.org/10.1063/1.4878483>

- Hrstka, T., Gottlieb, P., Skála, R., Breiter, K., Motl, D., 2018. Automated mineralogy and petrology-applications of TESCAN Integrated Mineral Analyzer (TIMA). *J. Geosci.* 63, 47–63. <https://doi.org/10.3190/jgeosci.250>
- Kern, M., Möckel, R., Krause, J., Teichmann, J., Gutzmer, J., 2018. Calculating the department of a fine-grained and compositionally complex Sn skarn with a modified approach for automated mineralogy. *Miner. Eng.* 116, 213–225. <https://doi.org/10.1016/j.mineng.2017.06.006>
- Kikongi, P., Salvas, J., Gosselin, R., 2017. Curve-fitting regression: improving light element quantification with XRF. *X-Ray Spectrom.* 46, 347–355. <https://doi.org/10.1002/xrs.2760>
- Kupka, N., Tolosana-Delgado, R., Schach, E., Bachmann, K., Heinig, T., Rudolph, M., 2020. R as an environment for data mining of process mineralogy data: A case study of an industrial rougher flotation bank. *Miner. Eng.* 146, 106111. <https://doi.org/10.1016/j.mineng.2019.106111>
- Leißner, T., Bachmann, K., Gutzmer, J., Peuker, U.A., 2016. MLA-based partition curves for magnetic separation. *Miner. Eng.* 94, 94–103. <https://doi.org/10.1016/j.mineng.2016.05.015>
- Li, L., Bian, Y., Zhang, X., Guan, Y., Fan, E., Wu, F., Chen, R., 2018. Process for recycling mixed-cathode materials from spent lithium-ion batteries and kinetics of leaching. *Waste Manag.* 71, 362–371. <https://doi.org/10.1016/j.wasman.2017.10.028>
- Li, Q., Sun, X., 2016. Silicon Anode Materials for Next Generation Lithium-Ion Batteries, Electronic Thesis and Dissertation Repository. 3910.
- Li, W., Yang, S., Liu, N., Chen, Y., Xi, Y., Li, S., Jie, Y., Hu, F., 2019. Study on vacuum pyrolysis process of cathode sheets from spent lithium-ion batteries, in: *Minerals, Metals and Materials Series*. Springer International Publishing, pp. 421–435. https://doi.org/10.1007/978-3-030-10386-6_49
- Liu, J., Wang, H., Hu, T., Bai, X., Wang, S., Xie, W., Hao, J., He, Y., 2020. Recovery of LiCoO₂ and graphite from spent lithium-ion batteries by cryogenic grinding and froth flotation. *Miner. Eng.* 148, 106223. <https://doi.org/10.1016/j.mineng.2020.106223>
- Lombardo, G., 2019. Effects of pyrolysis and incineration on the chemical composition of Li-ion batteries and analysis of the by-products. Chalmers University of Technology.
- Lu, J., Wu, T., Amine, K., 2017. State-of-the-art characterization techniques for advanced lithium-ion batteries. *Nat. Energy* 2, 1–13. <https://doi.org/10.1038/nenergy.2017.11>
- Ma, S., Jiang, M., Tao, P., Song, C., Wu, J., Wang, J., Deng, T., Shang, W., 2018. Temperature effect and thermal impact in lithium-ion batteries: A review. *Prog. Nat. Sci. Mater. Int.* <https://doi.org/10.1016/j.pnsc.2018.11.002>
- Ma, T., Xu, G.L., Li, Y., Wang, L., He, X., Zheng, J., Liu, J., Engelhard, M.H., Zapol, P., Curtiss, L.A., Jorne, J., Amine, K., Chen, Z., 2017. Revisiting the Corrosion of the Aluminum Current Collector in Lithium-Ion Batteries. *J. Phys. Chem. Lett.* 8, 1072–1077. <https://doi.org/10.1021/acs.jpcclett.6b02933>
- Malmgren, S., 2013. Insights into Li-ion Battery and Stainless Steel Interfaces Using Refined Photoelectron Spectroscopy Methodology. <https://doi.org/10.1016/j.electacta.2013.03.010>
- Manthiram, A., 2020. A reflection on lithium-ion battery cathode chemistry. *Nat. Commun.* <https://doi.org/10.1038/s41467-020-15355-0>
- Manthiram, A., 2017. An Outlook on Lithium Ion Battery Technology. *ACS Cent. Sci.* 3, 1063–1069. <https://doi.org/10.1021/acscentsci.7b00288>
- Mariano, R.A., Evans, C.L., 2015. Error analysis in ore particle composition distribution measurements.

Min. Eng.

- Mekonnen, Y., Sundararajan, A., Sarwat, A.I., 2016. A review of cathode and anode materials for lithium-ion batteries, in: Conference Proceedings - IEEE SOUTHEASTCON. Institute of Electrical and Electronics Engineers Inc. <https://doi.org/10.1109/SECON.2016.7506639>
- Or, T., Gourley, S.W.D., Kaliyappan, K., Yu, A., Chen, Z., 2020. Recycling of mixed cathode lithium-ion batteries for electric vehicles: Current status and future outlook. *Carbon Energy* 2, 6–43. <https://doi.org/10.1002/cey2.29>
- Otsuki, A., Mensbruge, L.D. La, King, A., Serranti, S., Fiore, L., Bonifazi, G., 2020. Non-destructive characterization of mechanically processed waste printed circuit boards - particle liberation analysis. *Waste Manag.* 102, 510–519. <https://doi.org/10.1016/j.wasman.2019.11.006>
- Pavoni, F.H., Sita, L.E., dos Santos, C.S., da Silva, S.P., da Silva, P.R.C., Scarminio, J., 2018. LiCoO₂ particle size distribution as a function of the state of health of discarded cell phone batteries. *Powder Technol.* 326, 78–83. <https://doi.org/10.1016/j.powtec.2017.12.059>
- Pereira, L., Birtel, S., Möckel, R., Michaux, B., Silva, A.C., Gutzmer, J., 2019. Constraining the economic potential of by-product recovery by using a geometallurgical approach: The example of rare earth element recovery at Catalão I, Brazil. *Econ. Geol.* 114, 1555–1568. <https://doi.org/10.5382/econgeo.4637>
- Pereira, L., Frenzel, M., Khodadadzadeh, M., Tolosana-Delgado, R., Gutzmer, J., 2020. A self-adaptive particle-tracking method for minerals processing. *J. Clean. Prod.* 279, 123711. <https://doi.org/10.1016/j.jclepro.2020.123711>
- Pinegar, H., Smith, Y.R., 2019. End-of-Life Lithium-Ion Battery Component Mechanical Liberation and Separation. *JOM* 71, 4447–4456. <https://doi.org/10.1007/s11837-019-03828-7>
- Poliakov, A., Donskoi, E., 2019. Separation of touching particles in optical image analysis of iron ores and its effect on textural and liberation characterization. *Eur. J. Mineral.* 31, 485–505. <https://doi.org/10.1127/ejm/2019/0031-2844>
- Porvali, A., Aaltonen, M., Ojanen, S., Velazquez-Martinez, O., Eronen, E., Liu, F., Wilson, B.P., Serna-Guerrero, R., Lundström, M., 2019. Mechanical and hydrometallurgical processes in HCl media for the recycling of valuable metals from Li-ion battery waste. *Resour. Conserv. Recycl.* 142, 257–266. <https://doi.org/10.1016/j.resconrec.2018.11.023>
- Quan, C., Li, A., Gao, N., 2012. Study on characteristics of printed circuit board liberation and its crushed products. *Waste Manag. Res.* 30, 1178–1186. <https://doi.org/10.1177/0734242X12457119>
- Rahfeld, A., Gutzmer, J., 2017. MLA-Based Detection of Organic Matter with Iodized Epoxy Resin—An Alternative to Carnauba. *J. Miner. Mater. Charact. Eng.* 05, 198–208. <https://doi.org/10.4236/jmmce.2017.54017>
- Røisi, I., Aasly, K., 2018. The effect of graphite filler in sample preparation for automated mineralogy—a preliminary study. *Miner.* 8. A1-A23 .
- Ross, B.J., LeResche, M., Liu, D., Durham, J.L., Dahl, E.U., Lipson, A.L., 2020. Mitigating the Impact of Thermal Binder Removal for Direct Li-ion Battery Recycling. *ACS Sustain. Chem. Eng.* <https://doi.org/10.1021/acssuschemeng.0c03424>
- Ruismäki, R., Rinne, T., Dańczak, A., Taskinen, P., Serna-Guerrero, R., Jokilaakso, A., 2020. Integrating Flotation and Pyrometallurgy for Recovering Graphite and Valuable Metals from Battery Scrap. *Metals (Basel)*. 10, 680. <https://doi.org/10.3390/met10050680>
- Sandmann, D., Gutzmer, J., 2013. Use of Mineral Liberation Analysis (MLA) in the Characterization

- of Lithium-Bearing Micas. *J. Miner. Mater. Charact. Eng.* 01, 285–292. <https://doi.org/10.4236/jmmce.2013.16043>
- Sandmann, D., Haser, S., Gutzmer, J., 2014. Characterisation of graphite by automated mineral liberation analysis. *Trans. Institutions Min. Metall. Sect. C Miner. Process. Extr. Metall.* 123, 184–189. <https://doi.org/10.1179/1743285514Y.0000000063>
- Sandmann, D., Jäckel, H.G., Gutzmer, J., 2019. Cues to greater recycling efficiency-characterization of a crushed mobile phone by mineral liberation analysis (MLA), in: *Materials Science Forum*. Trans Tech Publications Ltd, pp. 134–141. <https://doi.org/10.4028/www.scientific.net/MSF.959.134>
- Schulz, B., Sandmann, D., Gilbricht, S., 2020. SEM-Based Automated Mineralogy and its Application in Geo- and Material Sciences. *Minerals* 10, 1004. <https://doi.org/10.3390/min10111004>
- Shi, Y., Chen, G., Chen, Z., 2018. Effective regeneration of LiCoO₂ from spent lithium-ion batteries: A direct approach towards high-performance active particles. *Green Chem.* 20, 851–862. <https://doi.org/10.1039/c7gc02831h>
- Sun, L., Qiu, K., 2011. Vacuum pyrolysis and hydrometallurgical process for the recovery of valuable metals from spent lithium-ion batteries. *J. Hazard. Mater.* 194, 378–384. <https://doi.org/10.1016/j.jhazmat.2011.07.114>
- Theivaprakasam, S., Girard, G., Howlett, P., Forsyth, M., Mitra, S., Macfarlane, D., 2018. Passivation behaviour of aluminium current collector in ionic liquid alkyl carbonate (hybrid) electrolytes. *Nature* 2, 13. <https://doi.org/10.1038/s41529-018-0033-6>
- Tsai, P.C., Wen, B., Wolfman, M., Choe, M.J., Pan, M.S., Su, L., Thornton, K., Cabana, J., Chiang, Y.M., 2018. Single-particle measurements of electrochemical kinetics in NMC and NCA cathodes for Li-ion batteries. *Energy Environ. Sci.* 11, 860–871. <https://doi.org/10.1039/c8ee00001h>
- Ueda, T., Oki, T., Koyanaka, S., 2016. Statistical effect of sampling particle number on mineral liberation assessment. *Miner. Eng.* 98, 204–212. <https://doi.org/10.1016/j.mineng.2016.08.026>
- Velázquez-Martínez, Porvali, van den Boogaart, Santasalo-Aarnio, Lundström, Reuter, Serna-Guerrero, 2019. On the Use of Statistical Entropy Analysis as Assessment Parameter for the Comparison of Lithium-Ion Battery Recycling Processes. *Batteries* 5, 41. <https://doi.org/10.3390/batteries5020041>
- Velázquez-Martínez, Valio, Santasalo-Aarnio, Reuter, Serna-Guerrero, 2019. A Critical Review of Lithium-Ion Battery Recycling Processes from a Circular Economy Perspective. *Batteries* 5, 68. <https://doi.org/10.3390/batteries5040068>
- Versaci, D., Nasi, R., Zubair, U., Amici, J., Sgroi, M., Dumitrescu, M.A., Francia, C., Bodoardo, S., Penazzi, N., 2017. New eco-friendly low-cost binders for Li-ion anodes. *J. Solid State Electrochem.* 21, 3429–3435. <https://doi.org/10.1007/s10008-017-3665-5>
- Wang, F., Zhang, T., He, Y., Zhao, Y., Wang, S., Zhang, G., Zhang, Y., Feng, Y., 2018. Recovery of valuable materials from spent lithium-ion batteries by mechanical separation and thermal treatment. *J. Clean. Prod.* 185, 646–652. <https://doi.org/10.1016/j.jclepro.2018.03.069>
- Wang, Z., Dupré, N., Gaillot, A.C., Lestriez, B., Martin, J.F., Daniel, L., Patoux, S., Guyomard, D., 2012. CMC as a binder in LiNi_{0.4}Mn_{1.6}O₄ 5 v cathodes and their electrochemical performance for Li-ion batteries. *Electrochim. Acta* 62, 77–83. <https://doi.org/10.1016/j.electacta.2011.11.094>
- Warner, J., 2015. *The Handbook of Lithium-Ion Battery Pack Design*.
- Werner, D., Peuker, U.A., Mütze, T., 2020. Recycling chain for spent lithium-ion batteries. *Metals (Basel)*. 10. <https://doi.org/10.3390/met10030316>

- Widijatmoko, S.D., Gu, F., Wang, Z., Hall, P., 2020. Selective liberation in dry milled spent lithium-ion batteries. *Sustain. Mater. Technol.* 23. <https://doi.org/10.1016/j.susmat.2019.e00134>
- Writer, B., 2019. Anode Materials, SEI, Carbon, Graphite, Conductivity, Graphene, Reversible, Formation, in: *Lithium-Ion Batteries*. Springer International Publishing, pp. 1–71. https://doi.org/10.1007/978-3-030-16800-1_1
- Yen, J.-P., Chang, C.-C., Lin, Y.-R., Shen, S.-T., Hong, J.-L., 2013. Effects of Styrene-Butadiene Rubber/Carboxymethylcellulose (SBR/CMC) and Polyvinylidene Difluoride (PVDF) Binders on Low Temperature Lithium Ion Batteries. *J. Electrochem. Soc.* 160, A1811–A1818. <https://doi.org/10.1149/2.083310jes>
- Yoshio, M., Noguchi, H., 2009. A review of positive electrode materials for lithium-ion batteries, in: *Lithium-Ion Batteries: Science and Technologies*. Springer New York, pp. 9–48. https://doi.org/10.1007/978-0-387-34445-4_2
- Yudha, C.S., Muzayanha, S.U., Widiyandari, H., Iskandar, F., Sutopo, W., Purwanto, A., 2019. Synthesis of $\text{LiNi}_{0.85}\text{Co}_{0.14}\text{Al}_{0.01}\text{O}_2$ cathode material and its performance in an NCA/graphite full-battery. *Energies* 12. <https://doi.org/10.3390/en12101886>
- Zhang, G., Du, Z., He, Y., Wang, H., Xie, W., Zhang, T., 2019a. A sustainable process for the recovery of anode and cathode materials derived from spent lithium-ion batteries. *Sustain.* 11. <https://doi.org/10.3390/su11082363>
- Zhang, G., He, Y., Feng, Y., Wang, H., Zhu, X., 2018. Pyrolysis-Ultrasonic-Assisted Flotation Technology for Recovering Graphite and LiCoO_2 from Spent Lithium-Ion Batteries. *ACS Sustain. Chem. Eng.* 6, 10896–10904. <https://doi.org/10.1021/acssuschemeng.8b02186>
- Zhang, G., He, Y., Wang, H., Feng, Y., Xie, W., Zhu, X., 2019b. Application of mechanical crushing combined with pyrolysis-enhanced flotation technology to recover graphite and LiCoO_2 from spent lithium-ion batteries. *J. Clean. Prod.* 231, 1418–1427. <https://doi.org/10.1016/j.jclepro.2019.04.279>
- Zhang, S., Forssberg, E., 1999. Intelligent Liberation and classification of electronic scrap, in: *Powder Technology*. Elsevier Sequoia SA, pp. 295–301. [https://doi.org/10.1016/S0032-5910\(99\)00151-5](https://doi.org/10.1016/S0032-5910(99)00151-5)
- Zhang, W., Xu, C., He, W., Li, G., Huang, J., 2018. A review on management of spent lithium ion batteries and strategy for resource recycling of all components from them. *Waste Manag. Res.* 36, 99–112. <https://doi.org/10.1177/0734242X17744655>
- Zheng, Z., Chen, M., Wang, Q., Zhang, Y., Ma, X., Shen, C., Xu, D., Liu, J., Liu, Y., Gionet, P., O'Connor, I., Pinnell, L., Wang, J., Gratz, E., Arsenault, R., Wang, Y., 2018. High Performance Cathode Recovery from Different Electric Vehicle Recycling Streams. *ACS Sustain. Chem. Eng.* 6, 13977–13982. <https://doi.org/10.1021/acssuschemeng.8b02405>
- Zhu, S., He, W., Li, G., Zhou, X., Huang, J., Zhang, X., 2011. Recovering copper from spent lithium ion battery by a mechanical separation process, in: *ICMREE2011 - Proceedings 2011 International Conference on Materials for Renewable Energy and Environment*. pp. 1008–1012. <https://doi.org/10.1109/ICMREE.2011.5930972>
- Zielinski, M., Cassayre, L., Floquet, P., Macouin, M., Destrac, P., Coppey, N., Foulet, C., Biscans, B., 2020. A multi-analytical methodology for the characterization of industrial samples of spent Ni-MH battery powders. *Waste Manag.* 118, 677–687. <https://doi.org/10.1016/j.wasman.2020.09.017>
- Zou, H., Gratz, E., Apelian, D., Wang, Y., 2013. A novel method to recycle mixed cathode materials for lithium ion batteries. *Green Chem.* 15, 1183–1191. <https://doi.org/10.1039/c3gc40182k>